Obtención de mapas de temperatura de las anisotropías del fondo cósmico de microondas, correlacionadas y no-correlacionadas con la polarización

(Obtaining temperature maps of the Cosmic Microwave Background anisotropies, correlated and uncorrelated with polarization)

Trabajo de Fin de Máster
para acceder al

MÁSTER EN FÍSICA DE PARTÍCULAS Y DEL COSMOS

Autor: Laura Pérez Molina

Director\es: Patricio Vielva Martínez
Elena de la Hoz López-Collado

Julio - 2021

Abstract:

Recent observations of the Cosmic Microwave Background (CMB), particularly those provided by Planck, have detected some large-scale anomalies, with respect to what it is expected according to the standard cosmological model. With this in mind, this work presents a study on the possibility of defining new versions of the CMB temperature and E-mode polarization maps, which take into account the correlation/uncorrelation between them. These correlated and non-correlated parts can offer a new observable which could eventually increase the anomalous signal previously mentioned and, even, retrieve information about its unknown nature. For their obtention the construction and application of a Wiener filter to the CMB maps is needed. We study the impact that non-idealized maps (when they include instrumental noise, foreground residuals, or masked skies) can have when defining the filter and its efficiency. Another aspect to highlight, is that we have also studied the filter definition from given observations, without having to rely on previous knowledge given by a model. Finally, in an illustrative way, we analyse one possible application of the methodology to study one of the anomalies of the CMB: the lack of power on a large scale.

Keywords: Cosmic Microwave Background (CMB), Temperature, Polarization, Correlated / Uncorrelated Maps, CMB Anomalies.

Resumen:

Recientes observaciones del Fondo Cósmico de Microondas (FCM), particularmente las proporcionadas por Planck, han detectado una serie de anomalías a gran escala, con respecto a lo esperado según el modelo cosmológico estándar. Con esto en mente, este trabajo presenta un estudio sobre la posibilidad de definir mapas de la temperatura y del modo-E de polarización del FCM, que presentan correlación/no-correlación el uno con el otro. La razón es que esta descomposición entre partes correlacionadas y no-correlacionadas, pueden ofrecer un nuevo observable capaz de incrementar la señal anómala previamente mencionada e, incluso, arrojar luz sobre su naturaleza. La obtención de estos mapas radica en la aplicación de un filtro tipo Wiener. Se estudia el impacto que pueden tener mapas no idealizados, (cuando incluyen ruido instrumental, residuos de contaminantes, o una observación incompleta del cielo) a la hora de definir el filtro y su eficiencia. Otro aspecto a destacar, es que se estudia la viabilidad de definir el filtro a base de unas observaciones dadas, sin tener que basarse en el conocimiento previo de un modelo que defina las propiedades estadísticas de las observaciones. Por último, y a modo de ilustración, se estudia la posible viabilidad de aplicar esta metodología para estudiar una de las anomalías del FCM: la falta de potencia a gran escala.

Palabras clave: Fondo Cósmico de Microondas (FCM), Temperatura, Polarización, Mapas Correlacionados / No-correlacionados, Anomalías del FCM.

Contents

1 Introduction

Right after the Big Bang, the temperature of the Universe was so high that radiation was extremely intense. This translated into an opaque Universe where photons and baryonic matter collided with each other, preventing the formation of nuclei and consequently, matter was a hot ionized plasma. Around 380000 years after the Big Bang the energy, due to the expansion of the Universe, dropped enough so that the radiation decoupled from matter, leading to the constitution of the firsts atoms (mainly hydrogen). This period, when these first neutral atoms were formed, is known as *recombination epoch*. When the Universe's temperature reached approximately 3000 K, most protons had already recombined to form neutral atoms, which allowed the photons to travel freely. At that time the Universe became transparent. The radiation distribution of the decoupled photon follows a black-body spectrum, and corresponds nowadays to a temperature of $T_0 = 2.72548 \pm 0.00057$ K [1]. This isotropic radiation is known as the Cosmic Microwave Background (CMB).

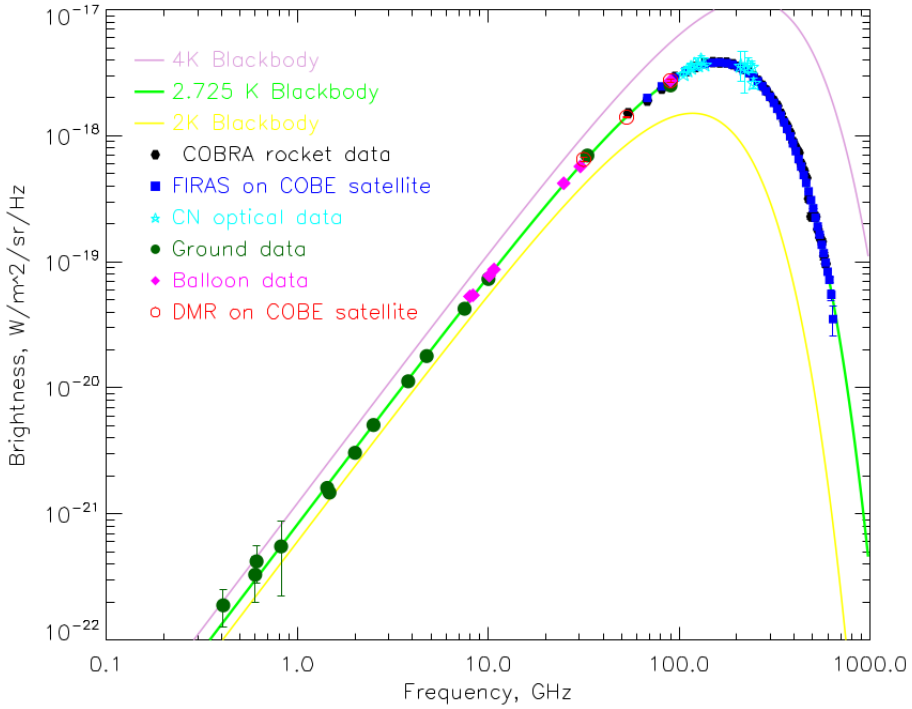

Figure 1: Expected black body curves for $T = 2$ K, $T = 2.725$ K and $T = 4$ K together with CMB measurements. Figure from [2].

In 1964 Penzias and Wilson discovered this relic radiation while trying to calibrate an antenna whose original purpose was to detect the reflection light bounced off Echo balloon satellites [3]. They detected an homogeneous and uniform radiation compatible with a background noise of ~ 3.5 K that was first interpreted as the CMB radiation in [4]. Years later, the CMB was measured at different frequencies with the FIRAS experiment [5] of the Cosmic Background Explorer (COBE) satellite , which verified that the radiation followed the black-body distribution theorized. This was a proof of the photon decoupling and an important evidence for the Big Bang theory. Besides, the DMR experiment [6] of the COBE satellite revealed that the CMB has fluctuations around T_0 on the order of 10^{-5} K. These anisotropies were later studied with higher precision by the Wilkinson Microwave Anisotropy Probe (WMAP) [7] and Planck [8] missions, which joined in 2001 and 2009 respectively. The fluctuations, although small, opened an interesting field of study, the CMB anisotropies. It is important to note that measuring them requires precise observations using sensitive detectors so that temperature differences smaller than 1 part in 10^5 can be determined.

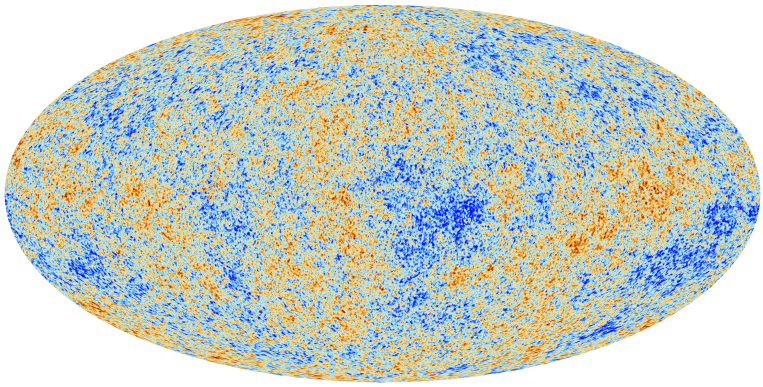

Figure 2: Temperature CMB fluctuations observed with Planck. Figure from the European Space Agency (ESA)[1].

Measurements of CMB temperature and polarization anisotropies encode lots of cosmological information such as the matter distribution or the Universe composition among others. Not only that, but they have resulted in the birth of Observational Cosmology and have also played a major role in establishing the standard ΛCDM cosmological model. The standard model of cosmology is a six-parameter model based on a flat Universe ($\Omega_k = 0$), dominated by a cosmological constant related to the dark energy (Λ) and cold dark matter (CDM), with initial gaussian, adiabatic fluctuations seeded by cosmic inflation. The six basic cosmological parameters are the baryon density[2] ($\Omega_b h^2$), the cold dark matter density ($\Omega_c h^2$), an approximation to the observed angular size of the sound horizon at recombination (θ_{MC}), the energy density perturbations amplitude (A_s) at $k = 0.05$ Mpc^{-1}, the spectral index of the corresponding power law (n_s) describing the size distribution of the primordial fluctuations, and the ionization optical depth (τ). The latter is related to the probability that a given microwave photon scatters with ionized electrons in the interstellar medium. There are other parameters, such as the tensor-to-scalar ratio (r), whose values can be constrained experimentally. The r parameter is typically defined as the ratio of the primordial power in density perturbations to that in tensor perturbations. We will assume $r = 0$ hereinafter. Last measurements provided by Planck revealed an upper limit of $r < 0.044$ at a 95% confidence level [9]. Observations have also confirmed the flatness of the Universe ($\Omega_k = 0$) and they have determined the Universe's energy content. We know that the Universe is in accelerated expansion at present $\Omega_\Lambda \sim 0.69$, with a matter content of only $\Omega_m \sim 0.31$ and a negligible contribution from radiation $\Omega_{rad} \approx 10^{-4}$. Table 1 summarizes the latest cosmological parameters from Planck [10].

Parameter	Planck data
Fit parameters:	
$\Omega_b h^2$	0.02242 ± 0.00014
$\Omega_c h^2$	0.11933 ± 0.00091
$100\theta_{MC}$	1.04101 ± 0.00029
τ	0.0561 ± 0.0071
n_s	0.9665 ± 0.0038
Derived parameters:	
H_0	(67.66 ± 0.42) km s^{-1} Mpc^{-1}
Ω_Λ	0.6889 ± 0.0056
Ω_m	0.3111 ± 0.0056
Age	(13.787 ± 0.020) Gyr

Table 1: Cosmological parameters obtained in the 68% limits for the base-ΛCDM model from Planck.

The CMB anisotropies are strongly tied to the existence of the large-scale structures (LSS) we

[1] `https://www.esa.int/ESA_Multimedia/Images/2013/03/Planck_CMB`

[2] Baryon density times h^2, where $H_0 = 100h$ km s^{-1} Mpc^{-1}.

observe in the present, e.g., galaxies, galaxy clusters, superclusters and beyond. These were seeded by spatial density fluctuations in the early Universe which appear in the CMB anisotropies[3]. Therefore LSS observations may also confirm the existence of primordial fluctuations in the early Universe. These primary CMB anisotropies are due to the gravitational redshift at large angular scales, and due to the evolution of the primordial photon-baryon evolution under gravity and Compton scattering at lower scales. Not only that, but we need to consider the fact that photons interact with cosmic structures in their way towards us. This effect is accounted in the secondary CMB anisotropies which can be classified into two types of interactions: (i) gravitational effects like the gravitational lensing or the integrated Sachs-Wolfe (ISW) effect; (ii) scattering effects such us the Sunyaev-Zel'dovich (SZ) effect, caused by inverse Compton interaction between photons and free electrons.

1.1 CMB Angular Power Spectra

The CMB anisotropies contain a lot of information on the statistical properties of the initial perturbations and the energy and matter content that governs the evolution of the Universe among others. All this information is encoded in **the angular power spectra of CMB anisotropies** which is a key observable and is described below [2, 11].

Since CMB is generated by random fluctuations, we can only predict its statistical properties as a function of angular size (assuming homogeneity and isotropy of the Universe). The temperature fluctuations we are going to analyse are projected in a 2D spherical surface and the most common description is given by expanding the temperature field using spherical harmonics ($Y_{\ell m}(\theta, \phi)$). We are interested in the deviations from the average temperature (T_0), and in general we will work with the dimensionless quantity that follows:

$$\Theta(\vec{x}, \eta, \theta, \phi) = \sum_{\ell=1}^{\infty} \sum_{m=-\ell}^{\ell} a_{\ell m}(\vec{x}, \eta) Y_{\ell m}(\theta, \phi) = \frac{T - T_0}{T_0}(\vec{x}, \eta, \theta, \phi). \tag{1.1}$$

Although this is defined at every point in space and time, we can observe it only here (at $\vec{x}_0 \equiv 0$) and now (at $\eta_0 \equiv 0$), where we can take this coordinates to be at the origin without loss of generality. This means that the only dependence that will be relevant in our anisotropies observations are the sky polar coordinates (θ, ϕ). The spherical harmonic functions are defined as:

$$Y_{\ell m}(\theta, \phi) = \sqrt{\frac{2\ell + 1}{4\pi} \frac{(\ell - m)!}{(\ell + m)!}} P_\ell^m(\cos\theta) e^{im\phi}. \tag{1.2}$$

The multipole describes its characteristic angular size ($\ell \in \mathbb{Z}^+$), the order m describes the angular orientations of a fluctuation mode ($-\ell \leq m \leq \ell$) and P_ℓ^m are the Legendre polynomials. These functions form a complete orthonormal set on the unit sphere as defined in the previous equation (1.2). This property can be derived from its normalization which can be written as:

$$\int_\Omega d\Omega \; Y_{\ell m}(\theta, \phi) Y^*_{\ell' m'}(\theta, \phi) = \delta_{\ell \ell'} \delta_{m m'}, \tag{1.3}$$

where Ω is the solid angle spanned by (θ, ϕ). We can invert equation (1.1) which shows the expansion of Θ in terms of the spherical harmonics by including equation (1.3) and integrating:

$$a_{\ell m} = \int_\Omega d\Omega \; \Theta(\theta, \phi) Y^*_{\ell m}(\theta, \phi), \tag{1.4}$$

We can only extract information of the distribution from which these $a_{\ell m}$ are drawn. The mean value of all $a_{\ell m}$'s is zero ($\langle a_{\ell m} \rangle = 0$). If we assume an isotropic field we can determine the *angular power spectrum* (C_ℓ) of these fluctuations as the variance of the harmonic coefficients,

$$\langle a_{\ell m} a^*_{\ell' m'} \rangle = C_\ell \delta_{\ell \ell'} \delta_{m m'}, \tag{1.5}$$

[3]Notice that the locations with matter overdensities (under-densities) show excess (lack) of temperature.

where the brackets denote an ensemble average over skies of the same cosmology. According to standard inflation scenarios, the CMB should be statistically isotropic, with perturbations that can be approximated as Gaussian. In this case, all the cosmological information is contained in these C_ℓ coefficients. Recalling the fact that the $a_{\ell m}$'s coefficients are drawn from the same distribution, for a given ℓ, each $a_{\ell m}$ has the same variance. As we can only measure $(2\ell+1)$ independent m-modes, we can estimate this power spectrum from the obtained maps as:

$$C_\ell = \frac{1}{2\ell+1}\sum_{m=-\ell}^{\ell} |a_{\ell m}|^2 \,, \tag{1.6}$$

which has associated an uncertainty denominated "cosmic variance", given by:

$$\sigma^2\left(C_\ell\right) = \frac{2}{(2\ell+1)} C_\ell^2 \ . \tag{1.7}$$

The cosmic variance is the most fundamental and inevitable source of uncertainty in the measurement of the CMB power spectrum. The quality of the average value estimation depends significantly on the sample size, the larger the later the closer to the actual value the estimation is. Figure 3 shows the D_ℓ [4] of the temperature measured with Planck and we can observe that the lower multipoles have larger uncertainties:

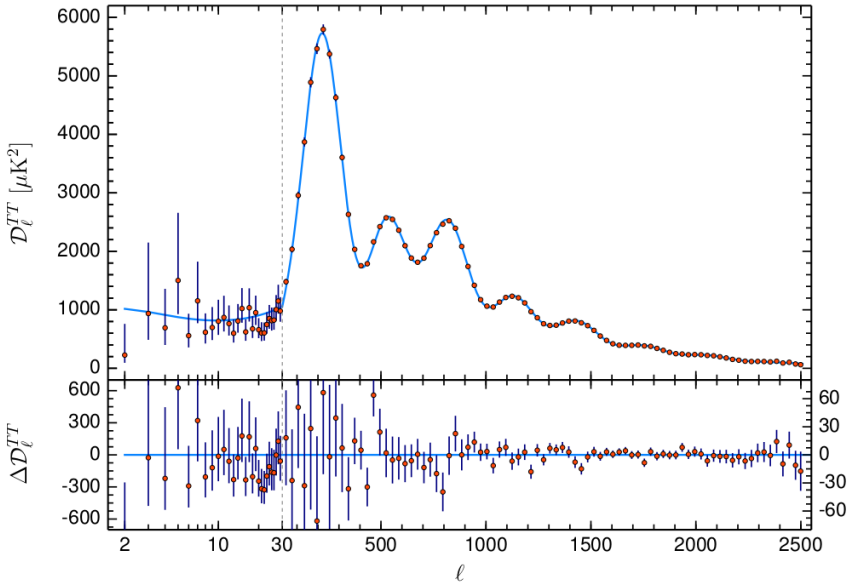

Figure 3: Planck 2018 temperature power spectrum [10]. The solid line represents the theoretical model based on ΛCDM and the residuals with respect to the best fit are shown in the lower panel.

The $\ell = 0$ term, the average CMB temperature, and the $\ell = 1$ term, the Doppler shift dominated by the motion of the Earth relative to the CMB, are usually removed for CMB analyses. Thus, the $\ell = 2$ term is the first one different from zero used. The region below $\ell \approx 20$ in Figure 3 is related to the primordial energy perturbation. At high ℓ values, we find the acoustic oscillations $(100 \lesssim \ell \lesssim 1000)$: (i) first peak ($\ell \sim 200$) reveals that the universe is close to spatially flat; (ii) the relative difference between the even and odds peaks tell us information about the amount of baryonic matter (on the second peak ($\ell \sim 500$); (iii) from the third peak ($\ell \sim 800$) to the damping tail we can obtain information of the dark matter and will provide consistency checks of underlying assumptions [2].

The CMB radiation is also linearly polarized and the measurement of this polarization is an important part of the current CMB research. The CMB polarization is generated by Thomson scattering of anisotropic radiation. This mechanism produces a fractional polarization of $\lesssim 10\%$.

[4] $D_\ell \equiv \ell(\ell+1)/(2\pi)C_\ell$ where C_ℓ is the original power spectrum.

For a quasi-monochromatic electromagnetic wave propagating in the direction $\hat{n}$, with arbitrary polarization, we can define [12]:

$$\mathrm{E}_i = a_i cos\left(\omega_0 t - \theta_i(t)\right) \quad \text{with} \quad i = 1, 2 \quad , \tag{1.8}$$

where E_i is the electric field[5] in the direction of the unit vector $\hat{e}_i$ which forms an orthonormal basis set with $\hat{n}$. The CMB radiation field is characterized by a 2×2 tensor and this lead to the definition of four parameters, the Stokes' parameters as:

$$I \equiv T = \langle |a_1|^2 \rangle + \langle |a_2|^2 \rangle, \tag{1.9}$$

$$Q = \langle |a_1|^2 \rangle - \langle |a_2|^2 \rangle, \tag{1.10}$$

$$U = \langle a_1 a_2 \cos(\theta_1 - \theta_2) \rangle, \tag{1.11}$$

$$V = \langle a_1 a_2 \sin(\theta_1 - \theta_2) \rangle. \tag{1.12}$$

The parameter T describes the absolute intensity, V measures the circular polarization and it is expected to be zero for the CMB, since Thomson scattering only induces linear polarization. At last, Q and U measure linear polarization and are used to parametrize the CMB polarization.

There are cases in which it may be useful to characterize polarization in different ways. The most intuitive and physical decomposition is a geometrical one, using the so-called the E- and B-modes, that are defined as linear combinations of Q and U parameters as:

$$(Q \pm iU)(\hat{n}) = \sum_{\ell=2}^{\infty} \sum_{m=-\ell}^{+\ell} a_{\ell m}^{\pm 2} \ {}_{\pm 2}Y_{\ell m}(\hat{n}) = \sum_{\ell=2}^{\infty} \sum_{m=-\ell}^{+\ell} (a_{\ell m}^{E} \pm i a_{\ell m}^{B}) \ {}_{\pm 2}Y_{\ell m}(\hat{n}), \tag{1.13}$$

where the E and B modes are defined by:

$$a_{\ell m}^{E} = \frac{1}{2}(a_{\ell m}^{+2} + a_{\ell m}^{-2}) \qquad , \quad a_{\ell m}^{B} = \frac{-i}{2}(a_{\ell m}^{+2} - a_{\ell m}^{-2}). \tag{1.14}$$

As mentioned before for the temperature anisotropies, a scalar field on the sphere can be expanded in spherical harmonics, $Y_{\ell m}(\theta, \phi)$, which form a complete and orthonormal basis. For the polarization we need to introduce another sets of functions to expand spin-s functions, the so called spin-weighted spherical spherical harmonics ${}_sY_{\ell m}$.These functions satisfy the same completeness and orthogonality relations,

$$\int_0^{2\pi} d\phi \int_{-1}^{1} d\cos\theta \ {}_sY^*_{\ell' m'}(\theta, \phi) \ {}_sY_{\ell m}(\theta, \phi) = \delta_{\ell' \ell} \delta_{m' m} \ , \tag{1.15}$$

$${}_sY^*_{\ell m} = (-1)^s \ {}_{-s}Y_{\ell -m} \ . \tag{1.16}$$

To describe the CMB polarization we have particularized these functions to the $s = 2$ case. It is important to note that these E- and B-modes are independent of the coordinate system chosen, contrary to Q and U. Not only that, but the primordial E-mode is a scalar magnitude generated by the initial energy density and tensor fluctuations (being the latter subdominant shown by current limits on r), while the primordial B-mode has only tensorial origin, which is related with the metric perturbations and the possible existence of primordial gravitational waves. Besides, gravitational lensing also transforms scalar perturbations from the E-modes to the B-modes. The important parameter for determining the strength of B-mode polarization is r, the tensor-to-scalar ratio. Moreover, we can define real space, spin-0 functions from these coefficients:

$$E_\ell(\theta, \phi) = \sum_m a_{\ell m}^{E} Y_{\ell m}(\theta, \phi) \quad , \quad B_\ell(\theta, \phi) = \sum_m a_{\ell m}^{B} Y_{\ell m}(\theta, \phi). \tag{1.17}$$

where it is found that E has even, $(-1)^\ell$, parity[6] and B has odd, $(-1)^{\ell+1}$, parity.

[5] Note the difference between the electric field, E_i, and the E-mode of polarization we will later define.

[6] Temperature has also even parity.

With this we can define a set of six angular power spectra, C_ℓ^{TT}, C_ℓ^{EE}, C_ℓ^{BB}, C_ℓ^{TE}, C_ℓ^{EB} and C_ℓ^{TB} as:

$$C_\ell^{XY} = \langle a_{\ell m}^X \left(a_{\ell m}^Y\right)^* \rangle = \frac{1}{2\ell+1} \sum_{m=-\ell}^{\ell} a_{\ell m}^X a_{\ell m}^{Y*} \quad , \text{ where } \quad X, Y \in \{T, E, B\}. \tag{1.18}$$

If we assume that the mechanisms involved in the formation of the CMB photons conserve parity, there will not be any coupling between B and T or E. Consequently, only four of the six combinations shown above are expected to be non-zero, and we assume $C_\ell^{EB} = C_\ell^{TB} = 0$.

The central goal for the Planck mission was to extract all of the information in the CMB anisotropies, allowing cosmological parameters to be determined to much higher accuracy. In order to extract cosmological information we need to measure the C_ℓ^{TT}, C_ℓ^{EE}, C_ℓ^{BB} and C_ℓ^{TE}. Whereas scalar perturbations amplified by the expansion, described by the ΛCDM model, only produce C_ℓ^{TT}, C_ℓ^{EE} and C_ℓ^{TE} spectra, the primordial gravitational waves perturbations can generate any of them. On the other hand, the amplitude of the primordial C_ℓ^{BB} given by the standard inflationary models is expected to be very small. Recall that the current limits in r are discussed when the cosmological parameters were introduced (Table 1). As mentioned before a C_ℓ^{BB} contribution from the E-mode has been also detected. The gravitational lensing effect accounts for the effect of distortion or bending of light rays that massive objects can produce when light passes near them. In this particular case, LSS produces the conversion between E and B modes[7] via gravitational lensing.

We will make use of `CAMB` code [13] (Code for Anisotropies in the Microwave Background), which allows us to study the anisotropies in the microwave background. It is a cosmology code for calculating CMB, lensing, galaxy count, dark-age 21cm angular power spectra, matter power spectra and transfer functions. In our case, we will use it as a Boltzmann equations solver to determine the CMB angular power spectra. Together with the cosmological parameters described in Table 1, we can determine these four power spectra and represent them in Figure 4.

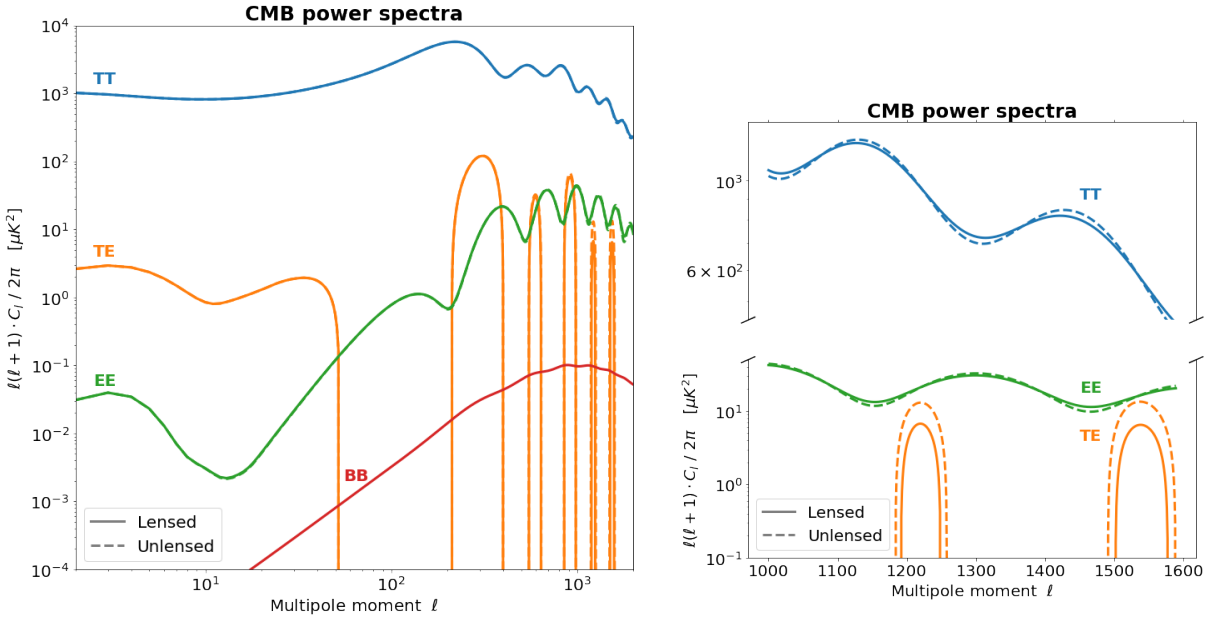

Figure 4: Temperature (blue), E-mode (green), B-mode (red) and T-E cross-correlation (orange). From Planck Cosmological Parameters [10] we obtain the angular power spectra with `CAMB` [13].

We represent the lensed and unlensed angular power spectra and so we can notice the gravitational lensing effect. Also it is important to notice that in our case $r = 0$, which implies that there are no tensorial modes leading to a null primordial C_ℓ^{BB}. As mentioned before, the LSS induced through the gravitational lensing effect a leakage from E-modes to B-modes . We can see in Figure 4 how this effect becomes significant at higher ℓ values.

[7]Note that the inverse conversion also takes place (from B to E mode) but is negligible in comparison.

1.2 Pixelization

From the theoretical cosmological model presented in the previous section we can reach a continuous description of the CMB signal. In practice, it is not feasible to measure the sky with infinite precision and so we need to introduce a partition of a spherical surface, i.e., a sky pixelization. Thus, the sky is divided into pixels on a sphere which allows to compute calculations with equal area pixels.

We will make use of the `healpy` package [14], a Python implementation of `HEALPix`[8] [15], which is a standard pixelation method to handle discrete data on the sphere. This module is usually applied in many analyses in astrophysics.

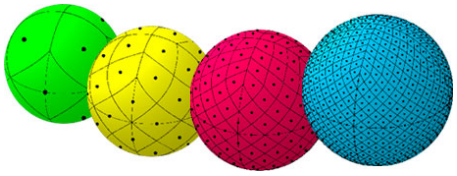

Figure 5: Diagram of the pixelation of the sphere made by `HEALPix` [15].

To promote the fast and accurate analysis of large full-sky data sets, `HEALPix` [15] provides a mathematical structure capable of performing discretizations of functions over the sphere. The three main properties, depicted in Figure 5, are: (i) the sphere is hierarchically divided into curvilinear quadrilaterals; (ii) areas of all pixels at a given resolution are identical; (iii) pixels are distributed on lines of constant latitude, which help decreasing the computational time involved in harmonic analyses. The resolution of these maps is given by the N_{side} parameter which is directly related to the number of pixels on a map as $N_{pix} = 12N_{side}^2$. Along the rest of the project we will use a resolution of $N_{side} = 512$.

1.3 Foregrounds & Instrumental Noise

In addition to the CMB signal, the microwave sky has other physical phenomena contributions. We will need to consider the instrumental noise and the astrophysical foregrounds that would be present even with an ideal receiver. In order to retrieve the cosmological information from the received signal we need to remove these contaminants. As the instrumental precision is improved, and therefore the noise contribution is reduced, which is the case of most recent satellites, the main source of uncertainty is the contamination by foreground emissions.

The main astrophysical foregrounds come from our Galaxy from four mechanisms: synchrotron radiation, radiation from electron-ion scattering (free-free emission), thermal dust emission and AME (Anomalous Microwave Emission) which has been theorized as possible spinning dust [16].

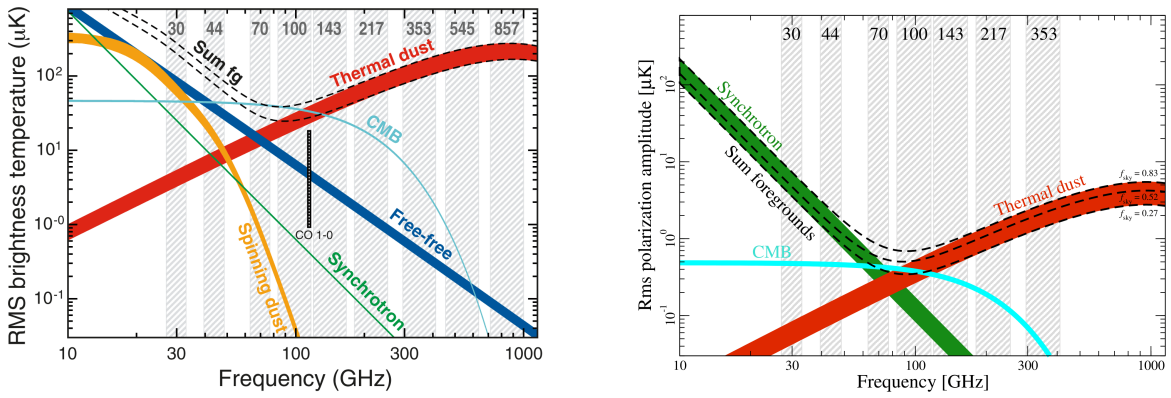

Figure 6: The root-mean-square intensity of each foreground compared with CMB temperature and polarization amplitudes. Figures from [17].

[8] Hierarchical Equal Area isoLatitude Pixelization of a sphere (`https://healpix.jpl.nasa.gov/`)

The synchrotron contribution to the foregrounds accounts for the emission from relativistic electrons interacting with cosmic rays and the magnetic fields present in the Galaxy. As we can see in Figure 6 this emission dominates at low microwave frequencies ($\lesssim$ 30 GHz). The spectral energy distribution is well described by a power-law. At higher frequencies ($\gtrsim$ 70GHz) thermal dust is the dominating component and describes the emission from the interstellar dust grains. It can be modelled as a modified black-body. Between these two components, the thermal free-free emission and AME become relevant. The free-free emission is also known as bremsstrahlung and arises from electron-ion scattering in the interstellar plasma. Besides, it has been shown that the contribution of carbon monoxide rotational transitions are significant, especially for the 100 GHz band [16].

Ideally we would like to remove these foregrounds to analyse the CMB temperature anisotropies. By performing observations at multiple frequencies one can perform component separation analyses to obtain the different components of this microwave sky.

On the other hand, we are going to consider Gaussian instrumental noise and assume, for simplicity, that the noise has a constant variance across all sky. Thus, the noise angular power-spectrum can be expressed as:

$$N_\ell \equiv \langle a_{\ell m}^{\text{Noise}} \left(a_{\ell' m'}^{\text{Noise}}\right)^* \rangle \delta_{\ell\ell'}\delta_{mm'} \Rightarrow \boxed{N_\ell = \frac{4\pi}{N_{pix}}(\sigma_{pix})^2} \quad , \tag{1.19}$$

where N_{pix} is the number of pixels in the map and σ_{pix} is related to the sensitivity of the satellite (in a pixel of area related to N_{pix}. This formula implies that the noise has a flat power spectrum ($N_\ell = \text{const.}$). There is no noise contribution to the cross-spectra as $N_\ell^{XY} = 0$ for $X \neq Y$ under the assumption of constant variance, with zero cross-correlation.

1.4 Motivation of this study

The variations in the CMB temperature maps at higher multipoles ($\ell \geq 2$) are interpreted as being mostly the result of perturbations in the density of the early Universe. The theoretical models used to describe the CMB generally predict that the $a_{\ell m}$ modes are Gaussian random fields to high precision as mentioned and assumed before. However, there have been some recents observations provided by Planck, showing mild deviations from this description, often referred as "anomalies". Some of these are the lack of power in the multipole range $\ell \simeq 20 - 30$, the "cold spot" or the power asymmetry between hemispheres [18, 19, 20]. Nevertheless, these deviations need to be confirmed with higher precision, as the available data only provide a $(2-3)\sigma$ discrepancy [10]. As we have seen in Figure 3, the cosmic variance at large scales limits the CMB study. To reduce these errors in the measurements the idea is to use the uncorrelated or correlated information with polarization provided by CMB anisotropies. It is known that the CMB presents anisotropies in temperature and polarization that are mostly independent and that the secondary anisotropies of the CMB can be detected using the cross-correlation between the LSS and the CMB temperature fluctuations. For this reason, we will analyse temperature and polarization maps trying to reduce the CMB uncertainty at large scales.

In [21] a method to reduce the noise by analysing the information contained in the polarization of CMB was proposed. Their objective was to study the integrated Sachs–Wolfe (ISW), and so they calculated the correlated and uncorrelated temperature maps and studied the reduction of the uncertainties. We will follow this idea, but in our case, aiming to have maps that would eventually help us to probe the origin of the CMB anomalies. We will translate the observed E-mode polarization maps into temperature maps using the E-mode angular cross-power spectrum. These temperature maps are then subtracted from the observed temperature maps, remaining the uncorrelated part of the maps which would have a smaller contribution to the uncertainty of the detected signal. The aim of the project is to obtain information from these correlated and uncorrelated temperature maps with the E-mode polarization[9], and so during the project we will mostly analyse C_ℓ^{TT}, C_ℓ^{EE} and C_ℓ^{TE} power spectra. We have also applied this methodology to sky maps simulations of future missions, in particular the LiteBIRD (Lite (Light) satellite for the studies of B-mode polarization and

[9]For completeness we will also study the E-mode polarization correlated with temperature.

Inflation from cosmic background Radiation Detection) mission. Although the primary objective of this satellite is the detection of primordial gravitational waves through the footprint left on the polarized CMB B-modes, LiteBIRD is expected to retrieve an E map with uncertainties on the order of the cosmic variance limit [22].

Once we have developed a methodology to obtain correlated and uncorrelated maps, we will use it to discern if it would allow us to detect with higher significance the mentioned anomalies. In our case, we will focus on the lack of power at large scales anomaly, which refers to the systematic reduction of the angular power spectrum measured at the low multipoles. This can be observed in Figure 3 in the multipoles $\ell \sim (20 - 30)$ where we show the temperature angular power spectrum measured by Planck.

The rest of the work is structured as follows: in section §2 we will explain how we have generated the simulations of the sky maps. These maps include CMB (§2.1), contaminants (§2.2, §2.4) and a mask (§2.3). In section 4Once we have the maps, we introduce the Wiener filter we will use to obtain the correlated and uncorrelated parts of the temperature maps with the E-mode polarization in section §2.5. In section §3 we present these correlated maps and how well we are able to recover the theoretical predictions depending on the contaminants level that is present in the simulations. Not only that, but we analyse the particular case where we only have one realization available and develop a method to obtain compatible results with the simulated ones. In section 4 we apply the developed methodology to a simple toy model case where we induce a lack of power in the E-mode at low multiples as well as the observed lack of power in T. Then, we try to infer whether more statistically significant conclusions can be extracted from the correlated and uncorrelated maps. Finally, we summarize the conclusions in section §5.

2 Simulations & Methodology

In this section we describe the data sets and the simulations used throughout the project. In subsection §2.1 we describe the CMB related data. The noise simulations are discussed in subsection §2.2 and in §2.4 we explain how foreground residuals are simulated. We dedicate a section (§2.3) to explain the masking procedure followed in this work to mitigate the effects of the foreground contamination, specially at the galactic disk. Finally, in subsection §2.5 we introduce the Wiener filter formalism that is latter used to obtain the correlated temperature with E-mode polarization maps and their complementary.

Our intention is to generate simulations of the CMB map obtained after component separation, i.e., after applying a pipeline to extract the CMB signal from the multi-frequency measured sky signal. These include noise and foreground residuals, i.e., a leftover signal from the foreground emission after component separation. It is useful to define the measured sky signal harmonic coefficients [12] as:

$$s^X_{\ell m} = \int X^{\rm map}(\Omega) Y^*_{\ell m}(\Omega) d\Omega \approx \sum_{j=1}^{N_{pix}} \frac{4\pi}{N_{pix}} X^{\rm map}_j Y_{\ell m}(\theta_j, \phi_j), \tag{2.1}$$

with $X^{\rm map}_j$ the jth pixel of the convenient map, located in the sky with coordinates (θ_j, ϕ_j). It is important to note that these measured coefficients include noise, foreground residuals, and beam and pixelization effects. Finally, the observed map is the sum of the cosmological signal (CMB), noise and foregrounds residuals:

$$s_{\ell m} = \left[a^{\rm CMB}_{\ell m} p_\ell b_\ell\right] + a^{\rm Noise}_{\ell m} + \left[a^{\rm Foreg}_{\ell m} p_\ell b_\ell\right]. \tag{2.2}$$

Considering no correlation between the cosmological signal and the noise we can express the angular power spectra as:

$$S^{XY}_\ell \equiv \langle s^X_{\ell m} s^{Y*}_{\ell' m'} \rangle = \left(\bar{C}^{XY}_\ell p^2_\ell b^2_\ell\right) + N^{XY}_\ell + \left(\bar{F}^{XY}_\ell p^2_\ell b^2_\ell\right) \ , \text{ where } X, Y \in \{T, E, B\}, \tag{2.3}$$

where p_ℓ is the pixel window function, which describes the effect that the pixelated resolution has on the sky signal, and b_ℓ is the beam window, which accounts for the smearing effect related with the finite beam width of any observing instrument. We assume a Gaussian shape for the beam, $b_\ell = \exp\left(-\ell(\ell+1)\sigma^2_b\right)$, where $\sigma_b = \theta_{\rm FWHM}/\sqrt{8\ln 2}$, and $\theta_{\rm FWHM}$ is the full-width at half-maximum (FWHM) of the beam. We assume that the noise is an uncorrelated Gaussian random variable, hence we can model its angular power spectra with the expression (1.19). We have also introduced a simplified notation: S^{XY}_ℓ is the total, $C^{XY}_\ell \equiv \left(\bar{C}^{XY}_\ell p^2_\ell b^2_\ell\right)$ refers to the CMB, N^{XY}_ℓ to the noise and $F^{XY}_\ell \equiv \left(\bar{F}^{XY}_\ell p^2_\ell b^2_\ell\right)$ to the foreground angular power spectra.

2.1 CMB simulations

As we have seen in section §1.1, CMB maps can be drawn as Gaussian random realizations of theoretical power spectra. We expect that all the information in the CMB can be described by D^{TT}_ℓ, D^{EE}_ℓ, D^{BB}_ℓ and D^{TE}_ℓ. We compute the CMB angular power spectra with `CAMB` package [13] and unless otherwise stated, we use the parameters shown in Table 1 to generate them. At last, we work with the maximum multipole value of $\ell_{max} = 3N_{side} - 1$. However, due to the known inaccuracies in the $a_{\ell m}$'s coefficients estimation beyond a given scale, all our representations are limited to $l_{plot} = 2N_{side}$

After computing the angular power spectra with `CAMB` we perform a set of 100 simulations of CMB realizations with `healpy.synalm` (i.e., the $a^{T,E,B}_{\ell m}$'s coefficients) and the associated temperature, E- and B-modes polarization maps using `healpy.alm2map` (we do not make use of B-mode in this work). This results in CMB maps with the same statistical properties as the real CMB map with the same initial power spectrum. To get similar maps to the experimental ones, we have convolved the $a_{\ell m}$ by the pixel window function and smoothed them given a `fwhm=30 arcmin` for the Gaussian beam window (typical value expected for LiteBIRD). We represent these two maps for one realization

with `healpy.mollview` in Figure 7. We can notice the difference in the order of magnitude of the signals of the maps, in the same way as observed with the CMB angular power spectra (Figure 4): the temperature is much higher than the polarization.

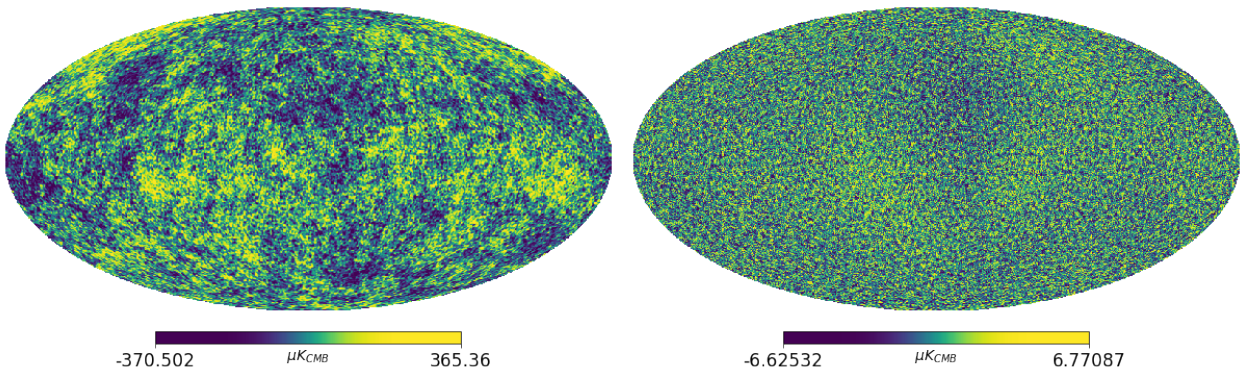

(a) Temperature CMB map.

(b) E-mode polarization CMB map.

Figure 7: CMB maps obtained with `healpy` from random realizations of theoretical power spectra.

Note that in the CMB maps shown in Figure 7 we have introduced a pixel window and a Gaussian beam window functions, characterized by p_X, b_X. To compare the simulated angular power spectra computed with `healpy.anafast` and the theoretical estimations given by `CAMB`, we include the windows functions in the theoretical description, $D_\ell^{\rm sim} \simeq D_\ell^{\rm CAMB}(p_X p_Y)(b_X b_Y)$. We represent them in Figure 8.

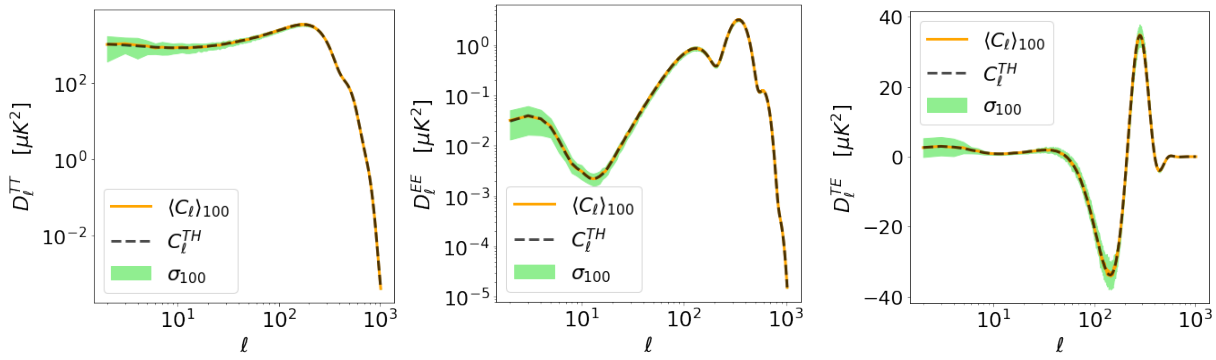

Figure 8: Angular power spectra obtained from the mean value of 100 simulations of CMB including pixel and Gaussian beam windows. We also show the theoretical result obtained with `CAMB` (dashed line) and the standard deviation (shaded).

2.2 White noise

The second ingredient to generate sky signal maps comparable with the observed ones is the instrumental noise. We generate the noise maps by associating a Gaussian realization, $\mathcal{N}(0, \sigma_X^2)$, to each map's pixel. The dispersion of the distribution is given by the sensitivity of the experiment we want to analyse. We take the LiteBIRD sensitivity that is expected to be around $\sigma_P = 2.6$ μK·arcmin for polarization observations [23]. This needs to be expressed per pixel unit, μK L_{pix}, where L_{pix} is defined as the length of the side of a square pixel at the given resolution. For that purpose we estimate the area given a resolution and then the number of pixels.

$$L_{pix} \sim \sqrt{A_{pix}} \frac{180}{\pi} 60 \quad \text{with} \quad A_{pix} \sim \frac{4\pi}{N_{pix}}, \tag{2.4}$$

$$\sigma_{pix}^P = \frac{\sigma_P}{L_{pix}} = \sigma_P \left(\sqrt{4\pi / N_{pix}} \frac{180}{\pi} 60 \right)^{-1} \quad , \quad \sigma_T = \frac{\sigma_P}{\sqrt{2}}, \tag{2.5}$$

where A_{pix} is the pixel area in stereo radians. We have assumed a temperature dispersion $\sqrt{2}$ lower than for polarization. Even so, it is important to recall that the LiteBIRD satellite is expected to recover the polarization signal with the lowest noise contribution so far. We represent a realization of temperature and E-mode polarization maps in Figure 9. We generate 100 noise simulations following the same procedure and we add them to the CMB simulations generated in section §2.1.

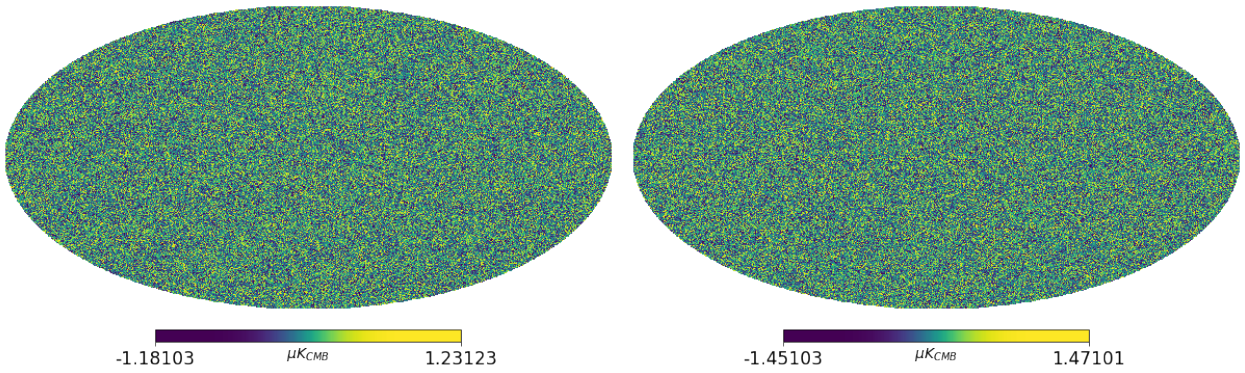

(a) Temperature noise map.

(b) E-mode polarization noise map.

Figure 9: Example of a realization of noise maps obtained introducing LiteBIRD sensitivity for temperature ($\sigma_T = \sigma_P/\sqrt{2}$ μK arcmin) and polarization ($\sigma_P = 2.6$ μK $\cdot$ arcmin) maps as Gaussian realizations.

We can particularize the expressions (2.2) and (2.3) for the case where we only have uncorrelated CMB and noise. We need to recall the theoretical model of the noise spectra shown in the equation (1.19), where the noise angular power spectra is constant and proportional to σ_X^2 and we have:

$$S_\ell^{XY} \equiv \langle s_{\ell m}^X s_{\ell m}^{Y*} \rangle = p_\ell^2 b_\ell^2 \bar{C}_\ell^{XY} + N_\ell^{XY} \begin{cases} S_\ell^{TT} = p_\ell^2 b_\ell^2 \bar{C}_\ell^{TT} + N_\ell^{TT} \\ S_\ell^{EE} = p_\ell^2 b_\ell^2 \bar{C}_\ell^{EE} + N_\ell^{EE} \\ S_\ell^{TE} = p_\ell^2 b_\ell^2 \bar{C}_\ell^{TE} \end{cases}, \tag{2.6}$$

We can notice that under the assumption of no correlation between the CMB and noise signals, the spectrum of the total map could be decomposed as the sum of the CMB and noise spectra. This is probed graphically in Figure 10, where we represent the CMB, the noise and the sum angular power spectra together with the total map power spectrum.

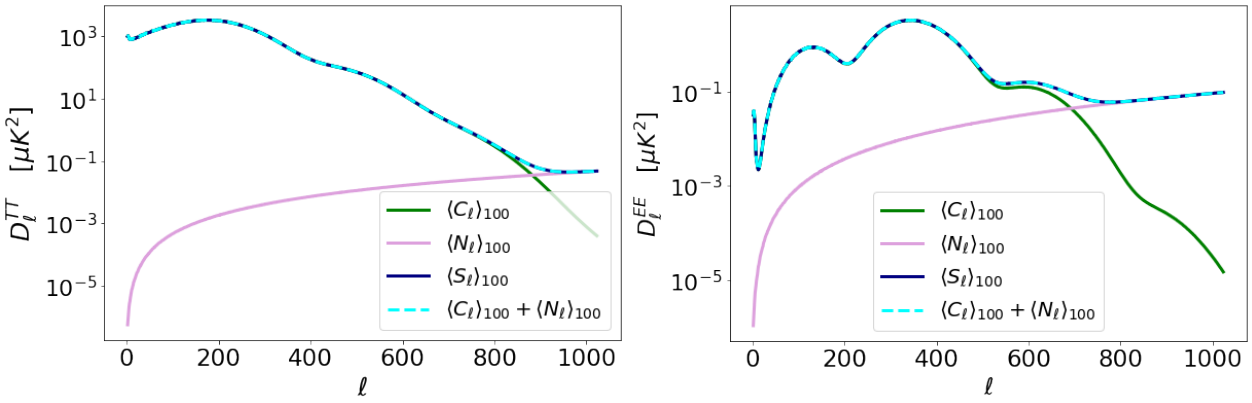

Figure 10: Mean spectra over 100 simulations of CMB, noise and the total maps. These total maps are constructed summing up the other two and allow us to confirm that there is no correlation between the CMB and the noise as indicated in the equation (2.6).

Not only that, but we expect that the T-E cross-angular power spectra does not have noise contribution. This can be checked with Figures 4 and 11 as they show the same spectra after including the noise model. In contrast to the temperature and E-mode polarization angular power spectra where we can notice the difference when including the noise maps at high multipoles ($\ell \sim 10^3$).

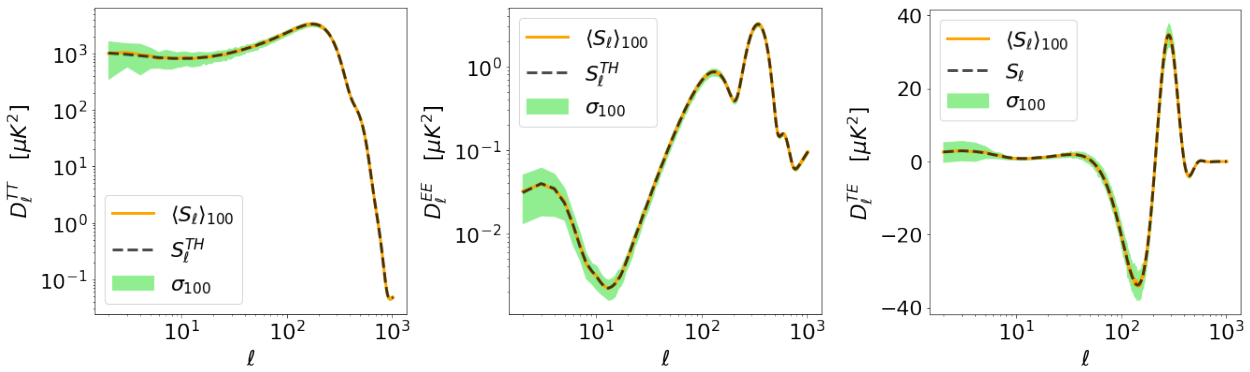

Figure 11: Angular power spectra obtained as the mean value of 100 simulations of CMB and noise. We include the theoretical models given by `CAMB` and by equation (1.19) for the CMB and the noise respectively (dashed line) and the standard deviation (shaded).

2.3 Masked maps

There could be some cases in which the contaminants of the sky signal have complex emissions and removing them to obtain the CMB signal is a challenging task. Generally, the need of masking some regions of the sky appears when the astrophysical foregrounds are included. As introduced in section §1.3, it is hard to model the foreground emission. This makes necessary a mask application for these regions, commonly located around the galactic disk. By convection, the masks are defined with zeros for masking the data and with ones where it is left unmasked. It should be noted that we introduce the masked maps before the foreground problem appears because we will need to mask the sky to obtain the residual foreground maps in section §2.4.

Although introducing the mask helps us solve the problem created by the foregrounds, it also raises new ones. The most noticeable is that the mask introduces correlations between the Q and U maps, and therefore in the E and B maps. Not only that, but it also may induce a coupling between the different multipoles. We need to consider all these effects when computing the power spectra of masked maps. As a first approximation we can neglect the effect of the mask on the angular power spectra and compute it with the `healpy.anafast` routine [14]. Ideally this calculation will be performed with a pseudo$-C_\ell$ estimator to remove the these effects, in our case with `NaMaster` [24]. This package takes into account the mask that has been applied to the map, and performs the needed corrections to the angular power spectra by computing the correlation matrix associated with the mask. To obtain even more precise results, sometimes it is necessary to perform a binning of the multipoles, mostly at the lower ones. With this, a weighted average over the multipoles in each bin is performed, reducing the effect of the cosmic variance of the lowest multipoles. We will use a binning scheme of 3 multipoles until $\ell = 8$, of 4 multipoles until $\ell = 20$, of 5 until $\ell = 90$ and the subsequent ones, one by one[10]. Moreover, we apodize the mask to include a gradual transition between the zeros and ones by convolving the mask with a Gaussian function. In order to choose the best apodization scale (in degrees), we perform a χ^2 analysis to determine the best value. We mask only-CMB maps with different apodization scales and the minimum is obtained for 5 degrees. This apodization scales is the sigma of the Gaussian distribution that is used to apodize the mask. Once we have determined the best configuration, we use the `NaMaster.mask_apodization` routine for the mask apodization. In Figure 12 we can see both the raw and the apodized masks.

[10]Recall that the monopole ($\ell = 0$) and dipole ($\ell = 1$) are not considered in the analysis.

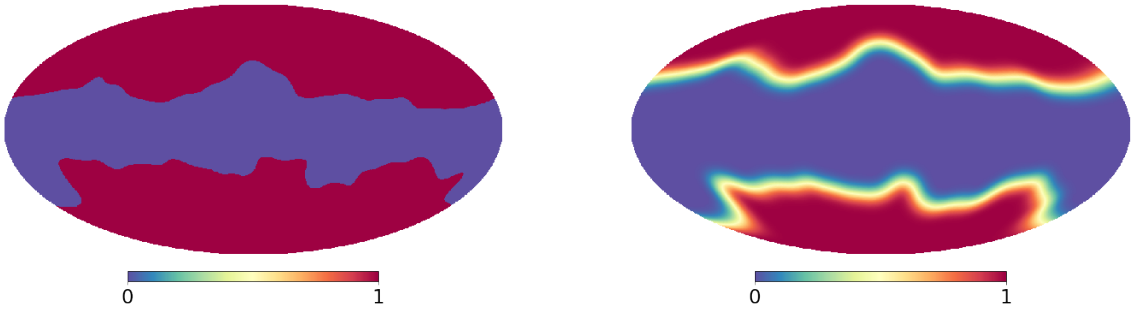

(a) Galactic mask with $f_{sky} = 60\%$.

(b) Apodized galactic mask with 5°.

Figure 12: Mask chosen for the analysis taken from the Planck Legacy Archive[11] with an $f_{sky} = 0.6$.

We can compute as an example the angular power spectra for the masked CMB and noise maps to see if it looks like the one shown in Figure 11, where we were considering full-sky maps.

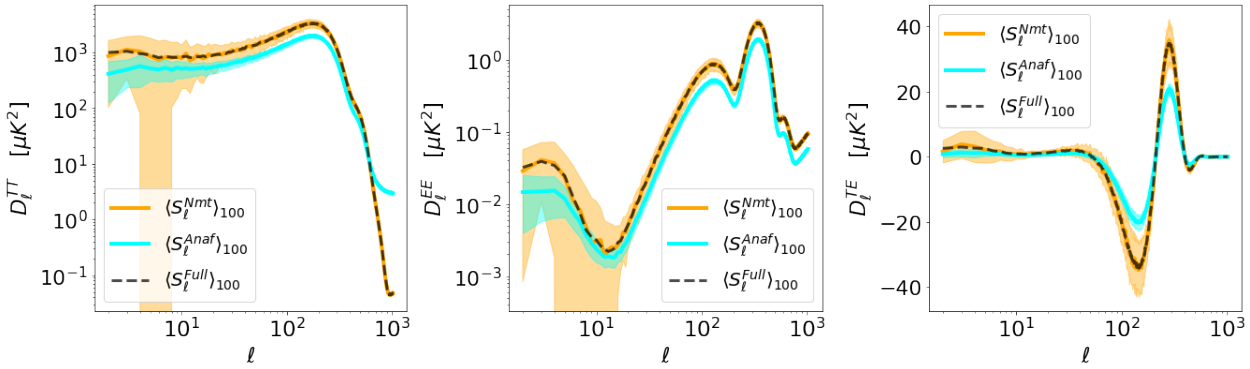

Figure 13: Angular power spectra obtained from the mean value of 100 simulations of CMB and noise. We include the obtained from the full-sky maps (dashed line),the computed with `NaMaster` (orange solid line) and `anafast` over the masked maps (cyan solid line). We also include the standard deviation (shaded) for the simulated angular power spectra.

As we note that the angular power spectra obtained with `NaMaster`, $\langle S_\ell^{\rm Nmt}\rangle_{100}$, recovers the spectra of the all-sky maps previously seen, $\langle S_\ell^{\rm Full}\rangle_{100}$, noting that the average value of 100 simulations have been performed. We can also represent the `healpy.anafast` angular power spectra estimation, and we can observe how they are affected by the mask. At first order, the difference is the fraction of the masked sky, although more differences are also present (associated to the mode coupling).

Finally, the effect of the mask needs to be included when estimating the uncertainties or cosmic variance, as the full-the sky is not available. In [25] it is shown that a good approximation for the error in the power spectrum can be obtained by dividing the cosmic variance shown in equation (1.7) by a factor of f_{sky}, the fraction of sky left uncovered by the mask

$$\sigma^2(C_\ell^{XX}) = \frac{2}{(2\ell+1)f_{sky}}\left(C_\ell^{XX}\right)^2. \tag{2.7}$$

This can be understood to be a result of information loss from masking a fraction $(1 - f_{sky})$ of the sky. If we would like to study the angular cross-power spectra we need to consider the following expression determined from the properties of the $a_{\ell m}$'s coefficients:

$$\sigma^2(C_\ell^{XY}) = \frac{[(C_\ell^{XY})^2 + C_\ell^{XX}C_\ell^{YY}]}{(2\ell+1)f_{sky}}. \tag{2.8}$$

[11] `http://pla.esac.esa.int/pla/#maps`

2.4 Foregrounds simulations

The last constituent of our maps are the foregrounds. We use the `PySM` package [26] to simulate full-sky Galactic foregrounds in temperature and polarization. We generate foregrounds-only frequency maps using the templates for thermal dust, synchrotron, AME and free-free emission (`"d1"`, `"s1"`, `"a1"`, `"f1"`). Notice that the free-free and AME emissions do not contribute to polarization although they may be relevant for the temperature maps. As we have seen in section §1.3 depending on the frequency we are working with, a different mechanism may be most important. In our case we generate the foreground maps according to the LiteBIRD specifications [23]. To compute these maps we need the frequency and sensitivity columns[12] which are summarized in Table 2, leading to 22 foreground maps (f_ν).

Telescope	Band ID	Center Frequency [GHz]	$\sigma_{P,ch}$ [μK · arcmin]
LFT	1	40	37.42
LFT	2	50	33.46
LFT	3	60	21.31
LFT	4	68	19.91
			31.77
LFT	5	78	15.55
			19.13
LFT	6	89	12.28
			28.77
LFT	7	100	10.34
MFT			8.48
LFT	8	119	7.69
MFT			5.70
LFT	9	140	7.25
MFT			6.38
MFT	10	166	5.57
MFT	11	195	7.05
HFT			10.50
HFT	12	235	10.79
HFT	13	280	13.80
HFT	14	337	21.95
HFT	15	402	47.45

Table 2: Parameters of the 2020 baseline design of LiteBIRD: band of frequencies and the expected noise ($\sigma_{P,ch}$) on the polarization signal on a sky pixel (see [23] for more details).

Once we have generated the foreground maps it is necessary to perform component separation analysis to get the residual contribution that will be added to the CMB temperature and E-mode polarization maps. As the component separation analysis is outside the scope of our work we will apply some known results and approximations. For that purpose we will determine the residual foreground contribution as the linear combination of the previously obtained frequency 22 maps, considering normalized weights.

$$f_R(x) = \sum_\nu f_\nu(t) w_\nu \quad \text{with} \quad w_\nu = \frac{a}{\sigma_P^2}\ ,\ \sum_\nu w_\nu = 1. \tag{2.9}$$

It is expected that, for LiteBIRD, after performing cleaning techniques the foreground contribution to the CMB temperature and E-mode polarization maps is negligible. According to [27, 28] the predicted residual level for LiteBIRD is:

$$M_\ell^B = 1.5 \cdot 10^{-4} \ell^{-2.29}. \tag{2.10}$$

[12]Note that there are frequencies that appear twice with different sensibilities and need to be considered separately.

We can assume that this level is similar for both E- and B- modes. With this we reescale the foreground residual maintaining the observed structure with:

$$a^X_{\ell m} = \hat{a}^X_{\ell m}\sqrt{\eta_B} \Rightarrow \boxed{F^{XY}_\ell = \hat{F}^{XY}_\ell \eta_B} \quad . \tag{2.11}$$

In order to account for the possible correlations between E and B the η_B parameter is defined as:

$$\eta_B = \left\langle \frac{M^B_\ell}{\tilde{F}^B_\ell} \right\rangle, \tag{2.12}$$

where $\tilde{F}^B_\ell \equiv \tilde{F}^{BB}_\ell$ is obtained as the masked foreground maps spectrum, $\tilde{F}^{XY}_\ell = \langle \tilde{a}^X_{\ell m} \tilde{a}^{Y*}_{\ell m} \rangle$, computed with `healpy.anafast`. As we have seen in Figure 13 the `healpy.anafast` estimation does not recover the full-sky angular power spectra and to correct this spectrum we divide by the f_{sky} factor.

We can represent these residual foreground maps with `healpy.mollview` in Figure 14.

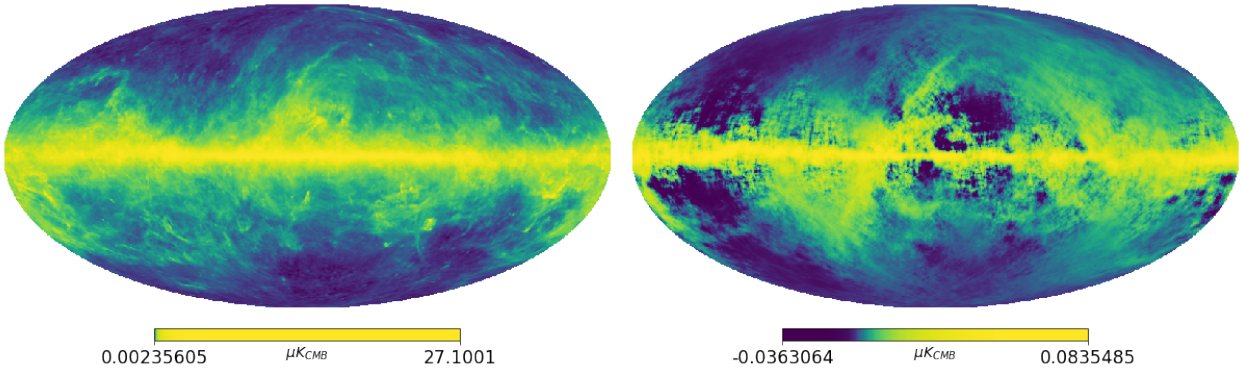

(a) Temperature map. (b) E-mode polarization map.

Figure 14: Residual foreground residual maps obtained and represented with `healpy` [14]. We use LiteBIRD band of frequencies shown in Table 2 to generate 22 foreground maps that lead to the residual ones after computing a linear combination and rescalling them according with the results from [27, 28]. (A non-linear scale has been used to observe the structure).

Once we have calculated all the components we can obtain after component separation CMB maps, henceforth CMB maps, which are composed by CMB (§2.1), instrumental noise (§simulations 2.2) and residual foreground maps (§2.4).We can represent the angular power spectra of these full-sky CMB maps and of each component to show graphically the different contributions to the equation (2.3).

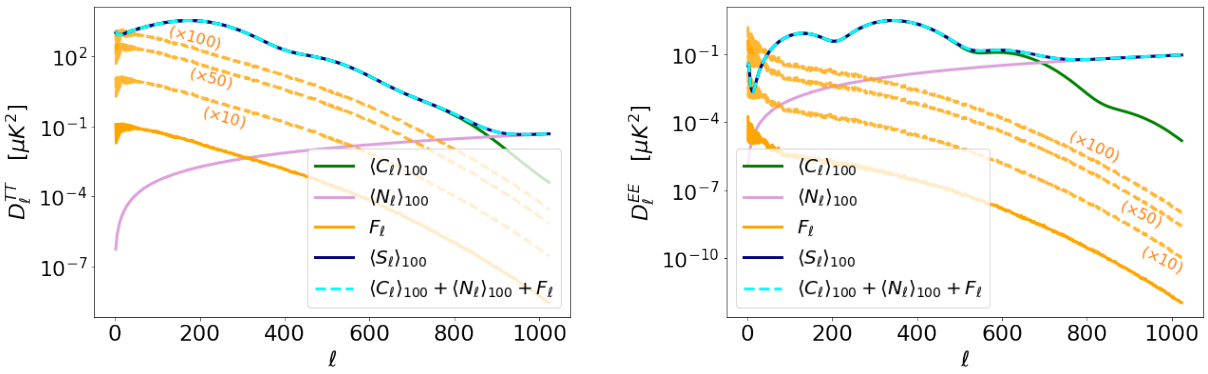

Figure 15: We represent the mean angular power spectra over 100 simulations for CMB, noise, foreground residuals and the total maps which are constructed summing up the other three. Besides the foreground residuals described in this section, for completeness we also represent additional levels that are considered in section §3.5.

Finally, we will apply the raw mask, presented in Figure 12a, to these maps to remove the galactic center as it is potentially the most contaminated region. The apodized mask shown in Figure 12b is used to compute the power spectrum with `NaMaster`.

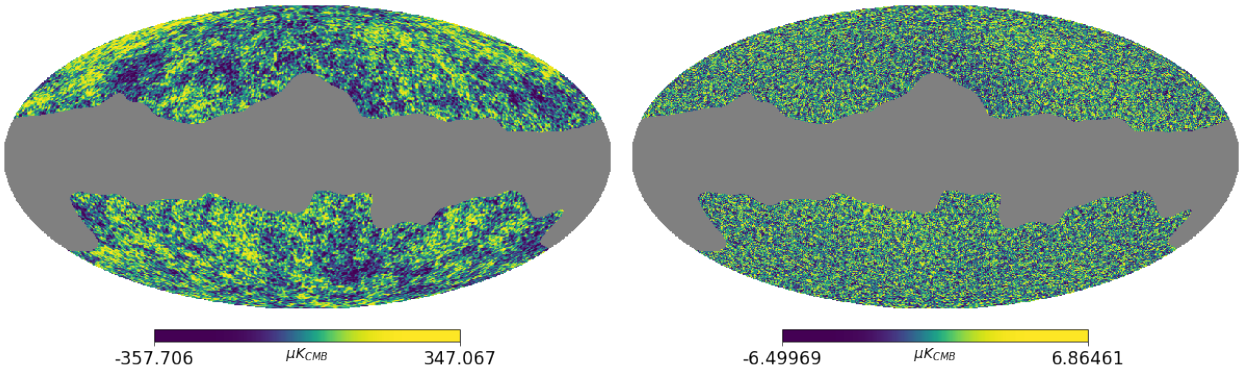

(a) Temperature map.

(b) E-mode polarization map.

Figure 16: Masked total maps with the raw mask of Figure 12a.

It is important to note that the foreground residuals are obtained following the indications given in [27, 28] and the employed mask has an $f_{sky} = 0.8$. However, as we have shown in section §2.3, the masks used during the analysis have an $f_{sky} = 0.6$. We have made this conservative decision not because it is necessary for analysing the results expected from LiteBIRD, but so we can consider greater deviations of the foreground residuals and also, because the complexity of the mask allow us to study the effect it has on other data in which the foreground residuals may be non-negligible, like for example in Planck observations.

2.5 Wiener filter

The CMB temperature anisotropies can be separated in a correlated and an uncorrelated part with polarization according to ΛCDM, and one can act as an uncertainty source to the other by contributing to the cosmic variance. With regard to the anomalies studies, sometimes the relevant information might be encoded in either the correlated or the uncorrelated part. Thus, we are interested in obtaining both the correlated and uncorrelated contributions independently to reduce the intrinsic sources of uncertainty and draw statistically more significant conclusions.

In practice, we will separate the temperature maps in two components: an E-correlated (TcE) and an E-uncorrelated ($TncE$) part. The definition of the uncorrelated temperature map and its angular power spectrum is given in [21] as:

$$a_{\ell m}^{TncE} = a_{\ell m}^{T} - \frac{C_\ell^{TE}}{C_\ell^{EE}} a_{\ell m}^{E} = a_{\ell m}^{T} - a_{\ell m}^{TcE} \quad \text{and} \quad C_\ell^{TncE} = C_\ell^{T} - \frac{\left(C_\ell^{TE}\right)^2}{C_\ell^{EE}}. \tag{2.13}$$

The polarization map $a_{\ell m}^{E}$ is correlated with the temperature fluctuations via C_ℓ^{TE}, and so it contains information about the temperature map. This can be translated into a correlated map of the temperature map with $(C_\ell^{TE}/C_\ell^{EE})a_{\ell m}^{E}$. It is later subtracted from the observed temperature map and remains the uncorrelated temperature fluctuations, $a_{\ell m}^{TncE}$. It can be seen in [21] that with this method the variance is reduced in every mode by the term $(C_\ell^{TE})^2/C_\ell^{EE}$. For completeness we will also consider the E-mode polarization correlated (EcT) and uncorrelated ($EncT$) maps with temperature, which are defined analogously as:

$$a_{\ell m}^{EncT} = a_{\ell m}^{E} - \frac{C_\ell^{TE}}{C_\ell^{TT}} a_{\ell m}^{T} = a_{\ell m}^{E} - a_{\ell m}^{EcT} \quad \text{and} \quad C_\ell^{EncT} = C_\ell^{E} - \frac{\left(C_\ell^{TE}\right)^2}{C_\ell^{TT}}. \tag{2.14}$$

Summing up all this information we can express the Wiener filter and the correlated part of a given

map in a general case as:

$$\boxed{w_\ell^X = \frac{C_\ell^{XY}}{C_\ell^{XX}} \quad \text{and} \quad a_{\ell m}^{XcY} = a_{\ell m}^Y w_\ell^Y} \quad . \tag{2.15}$$

Neglecting the effects of the contaminants, we can analyse how much the variance gets reduced in the different multipoles. In Figure 17 we can see the CMB temperature and E-mode polarization power spectrum C_ℓ^X, the correlated $C_\ell^X - (C_\ell^{XY})^2/C_\ell^{YY}$ and the uncorrelated $(C_\ell^{XY})^2/C_\ell^{YY}$ parts.

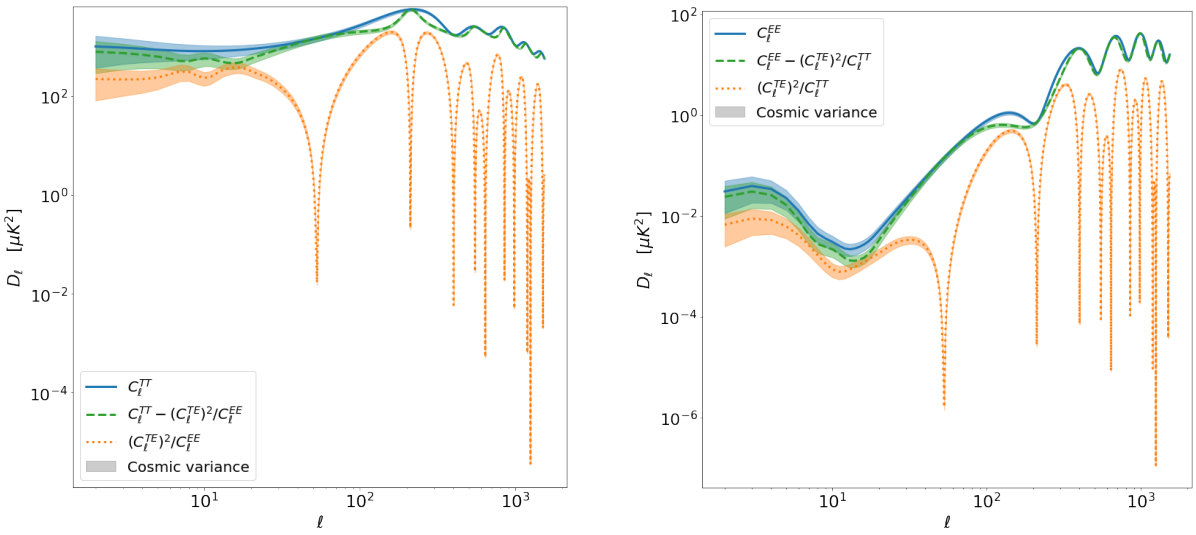

Figure 17: Theoretical CMB temperature and E-mode angular power spectra (solid line), the correlated (dotted line), the uncorrelated parts (dashed line) obtained with `CAMB` [13]. We can see in [21] an analogous figure for the temperature maps. Note that also shows the reduction factor of the variance by using the information contained in the polarization or temperature (dotted lines).

We observe that the signal of the TcE map is higher than the obtained in the EcT map. Certainly the C_ℓ^{TT} spectra is higher than the C_ℓ^{EE} and the angular cross-power spectra of the numerator is the same in both cases. This explains why most of the studies so far addressed in the literature are focused on the temperature correlated maps.

Although this approximation is useful to have a better understanding on the method for reducing the uncertainties, it is important to remember that the observations may contain instrumental noise and foregrounds. If we consider this general situation, the Wiener filter by [29]:

$$w_\ell^X = \frac{C_\ell^{XY} + F_\ell^{XY}}{C_\ell^{XX} + N_\ell^{XX} + F_\ell^{XX}}, \tag{2.16}$$

with C_ℓ, N_ℓ and F_ℓ representing the angular power spectra of CMB, noise and residual foregrounds, respectively. With this the XcY maps can be express as:

$$\Theta_{XcY}(\theta,\phi) = \sum_{\ell=0}^{l_{max}} \sum_{m=-l}^{l} a_{\ell m}^{XcY} Y_{\ell m}(\theta,\phi). \tag{2.17}$$

Then the $XncY$ map is build by subtraction, $\Theta_{XncY}(\theta,\phi) = \Theta_X - \Theta_{XcY} = \sum a_{\ell m}^{XncY} Y_{\ell m}$.

At last, we can analyse the relevance of the contaminants in the Wiener filter defined in (2.16). For this purpose we study the change with respect to the ideal filter when the contaminants are added. We can start by analysing the noise contribution that is parametrized with $n \in [0,1]$ and therefore the difference between the ideal filter and the one including noise is quantified by:

$$N(n) = 1 - \sum_{\ell=2}^{\ell_{max}} \frac{w_\ell(n)}{w_\ell(n=0)} \frac{1}{\ell_{max}-1} \quad \text{with} \quad w_\ell(n) = \frac{C_\ell^{XY}}{C_\ell^{XX} + nN_\ell^{XX}} \ . \tag{2.18}$$

We plot this function in Figure 18 which shows the low level of noise in future LiteBIRD observations. In both cases the differences between the filter when noise is included is almost negligible in all the n range. However, we can notice that for the temperature maps the noise level of LiteBIRD is even smaller than for the E-mode polarization maps. This can be explained by recalling the fact that the noise dispersion and contribution to the CMB is smaller for the temperature and moreover the angular power spectrum C_ℓ^{TT} is order of magnitude higher than C_ℓ^{EE}.

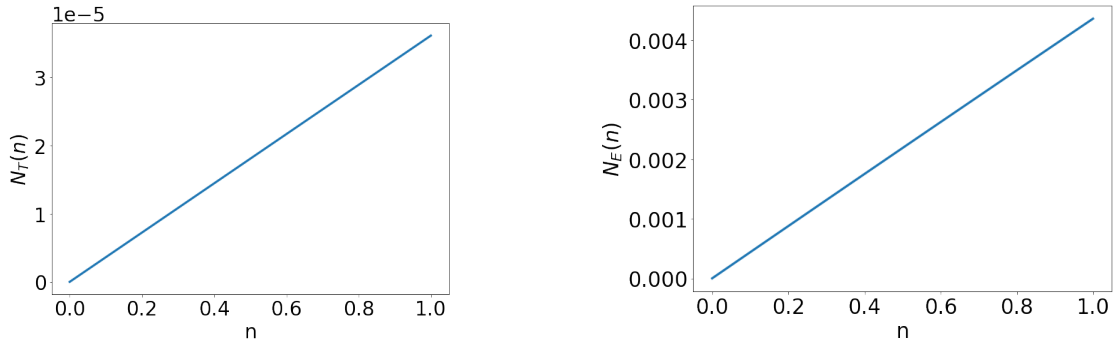

Figure 18: Difference with respect to the ideal filter when including noise. The x-axis (n) represents the reduction fraction applied to the noise angular power spectra, meaning for example $n = 0.2$ a reduction of the 80% with respect to the initial.

We can conclude that even if we could not suppress the noise contribution the difference with respect to the ideal filter is smaller than 0.5% for the w_ℓ^E filter definition and even smaller for the w_ℓ^T.

An analogous study can be performed to analyse the relevance of the foregrounds. We introduce the amplitudes f and g, which parametrize the reduction fraction of foreground residuals for X and Y modes respectively, reaching:

$$F(f,g) = 1 - \sum_{\ell=2}^{\ell_{max}} \frac{w_\ell(f,g)}{w_\ell(f=g=0)} \frac{1}{\ell_{max}-1} \quad \text{with} \quad w_\ell(f,g) = \frac{C_\ell^{XY} + (fg)F_\ell^{XY}}{C_\ell^{XX} + N_\ell^{XX} + f^2 F_\ell^{XX}}. \tag{2.19}$$

We show these functions in Figure 19 where, for simplicity, we have assumed that the reduction in the temperature and E-mode polarization foregrounds is given by the same parameter, $f = g$.

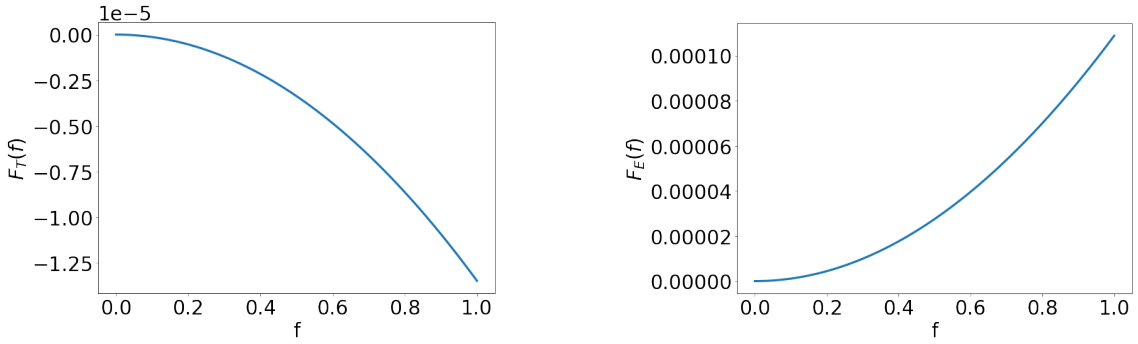

Figure 19: Difference with respect to the ideal filter when including foreground residuals.

In this case, we can notice that certainly the foreground residual level is negligible in both cases, as the difference we will introduce if we could not reduce them is of the 0.01% order for the E-mode polarization, and even smaller for the temperature.

3 Results & Analysis

In this section we present the correlated and uncorrelated temperature and E-mode maps obtained from the different data sets previously exposed. We analyse first the correlated maps obtained from CMB-only maps (§3.1) and later on we add contaminants in order to forecast the results that could be obtained from LiteBIRD observations. The main objective is to find an optimal way to compute the filter for either the simulations or data cases. We have worked with 100 simulations to extract conclusions. However, notice that actual observations of CMB experiments only provide information about our Universe (i.e. only one realization). In order to obtain results compatible with the observations, we have also considered the case where we only have one realization. To tackle this problem we develop a smooth method to handle the observed angular power spectra in section §3.4. The expected result is a smoothed filter in agreement with the results obtained from simulations and which will be used to get the correlated maps in a realistic scenario. Our final goal is to apply this smooth filter to obtain correlated maps of CMB maps after component separation, which include noise and foregrounds (§3.5). Not only that, but we would like to determine if it is possible to extract conclusions without being conditioned by a theoretical model. This is useful for the cases in which we can not model all the received emission, for example when foreground emission is not negligible. As a final goal, this method for smoothing the measured angular power spectra would eventually allow us to extract information of the underlying cosmological model directly from the observations.

3.1 Correlated maps from CMB simulations

From the 100 CMB ideal simulations generated as indicated in section §2.1, where neither noise nor foregrounds are taken into account, we can compute the Wiener filter defined in the equation (2.15). As we have included the pixel and the Gaussian beam window functions, we need to include these parameters to compare the simulated and theoretical filters, leading to the following expression:

$$w_X^{\rm th} = \frac{\tilde{C}_\ell^{XY}(p_X p_Y b_X b_Y)}{\tilde{C}_\ell^{XX}(p_X^2 b_X^2)} \quad \text{with} \quad \tilde{C}_\ell \equiv C_\ell^{\rm CAMB}. \tag{3.1}$$

We can represent both theoretical and simulated filters and observe how the mean simulated filter recovers the theoretical prediction.

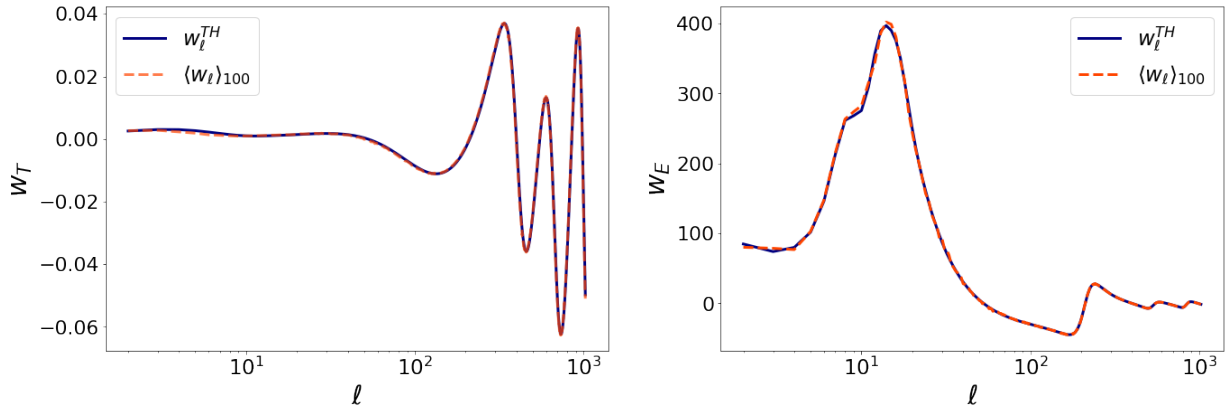

Figure 20: Wiener filters for CMB maps. The solid line represents the theoretical model given by equation (3.1) and the dashed line represents the mean filter obtained over 100 CMB simulations.

Once the filter has been computed we can apply it to the CMB maps to get the correlated and uncorrelated maps, which angular power spectra is given by:

$$D_\ell^{XcY} \simeq \frac{\left[\tilde{D}_\ell^{XY}(p_X p_Y b_X b_Y)\right]^2}{\tilde{D}_\ell^{YY}(p_Y^2 b_Y^2)}, \quad D_\ell^{XncY} \simeq \tilde{D}_\ell^{XX}(p_X^2 b_X^2) - \frac{\left[\tilde{D}_\ell^{XY}(p_X p_Y b_X b_Y)\right]^2}{\tilde{D}_\ell^{YY}(p_Y^2 b_Y^2)}. \tag{3.2}$$

Ideally we will always choose the theoretical filter to obtain the full-sky correlated maps. In this case, from the CMB simulations we obtain the spectra shown in Figure 21. There are differences at large-scales where the cosmic variance is greater and consequently the errors may be greater too.

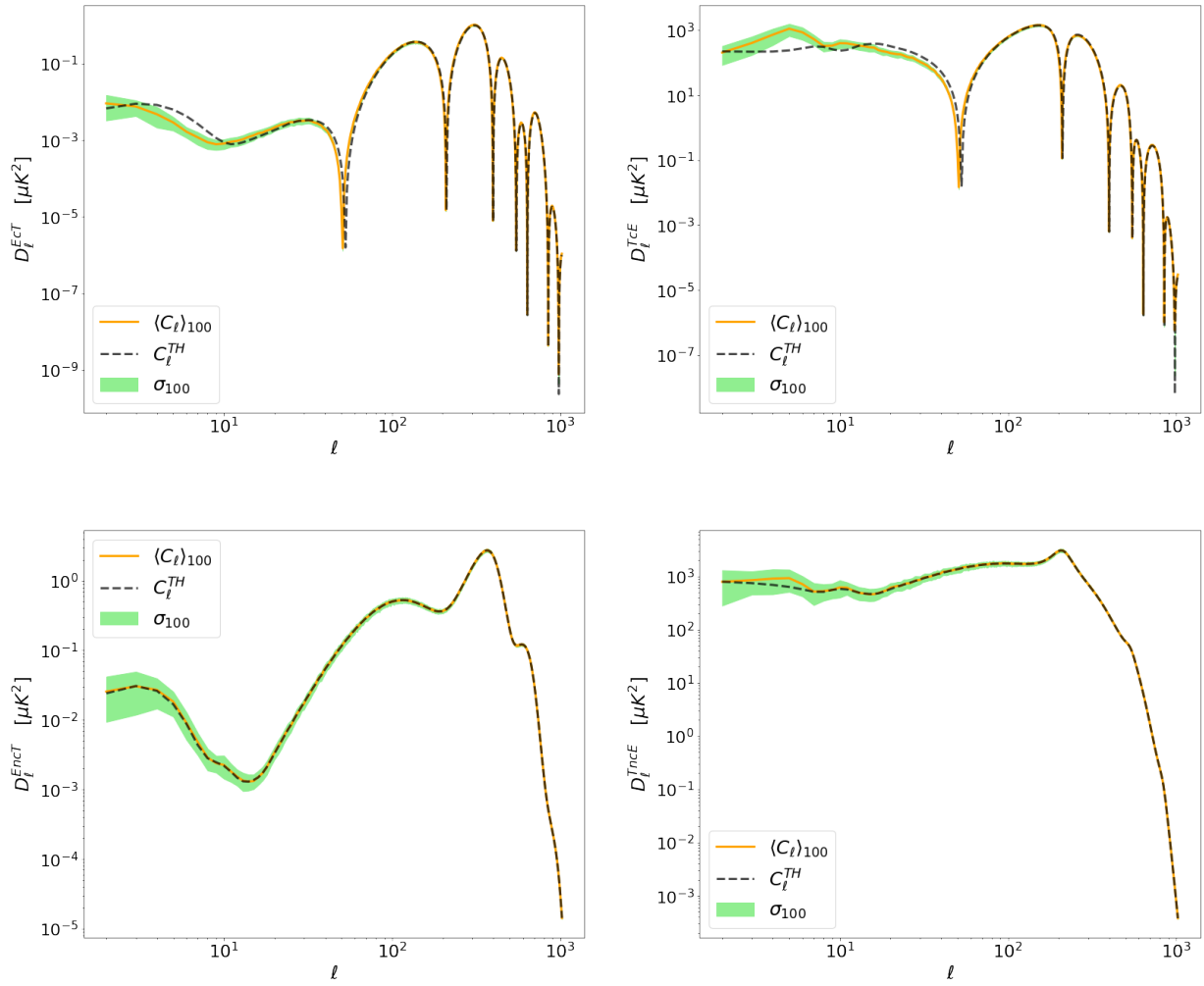

Figure 21: From CMB simulated maps, we obtain the correlated and uncorrelated parts for the temperature and E-mode polarization maps. We can see the theoretical result obtained with `CAMB` (dashed line), the mean over 100 simulations (solid line) and the standard deviation (shaded).

3.2 Correlated maps from CMB & noise simulations

As a first approximation to the observed CMB maps we include the existence of noise, in our case the instrumental noise for LiteBIRD as introduced in section §2.2. The filter definition is modified by including this contribution as:

$$w_X^{\rm th} = \frac{\tilde{C}_\ell^{XY}(p_X p_Y b_X b_Y)}{\tilde{C}_\ell^{XX}(p_X^2 b_X^2) + \tilde{N}_\ell^{XX}}. \tag{3.3}$$

We can represent the theoretical and simulated filters in this case, and we can notice that the simulations recover the theoretical estimation except at high ℓ values in the temperature filter, w_ℓ^T (Figure 22). This is explained by noticing that at this multipole range the noise is not completely canceled in the C_ℓ^{TE} of simulations and the signal is amplified with the C_ℓ^{TT} present in the denominator. Note that this happens due to the small power induced by the beam convolution. Otherwise, if the window functions were not included, the effect would have been reduced.

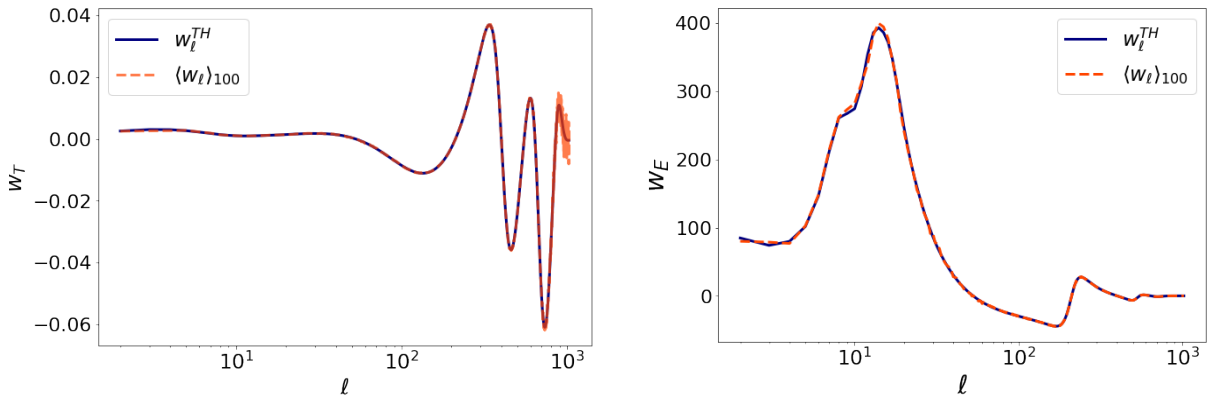

Figure 22: Wiener filters for CMB and noise maps. The solid line represents the theoretical model given by equation (3.3) and the dashed line represents the mean filter over the 100 CMB and noise simulations.

This filter is applied to CMB and noise maps, and we obtain the correlated and uncorrelated maps as in the previous case. The angular power spectra of these maps is given by:

$$D_\ell^{XcY} \simeq \frac{\left[\tilde{D}_\ell^{XY}(p_X p_Y b_X b_Y)\right]^2}{\tilde{D}_\ell^{YY}(p_Y^2 b_Y^2) + \tilde{N}_\ell^{YY}}, \quad D_\ell^{XncY} \simeq \tilde{D}_\ell^{XX}(p_X^2 b_X^2) - \frac{\left[\tilde{D}_\ell^{XY}(p_X p_Y b_X b_Y)\right]^2}{\tilde{D}_\ell^{YY}(p_Y^2 b_Y^2) + \tilde{N}_\ell^{YY}}. \tag{3.4}$$

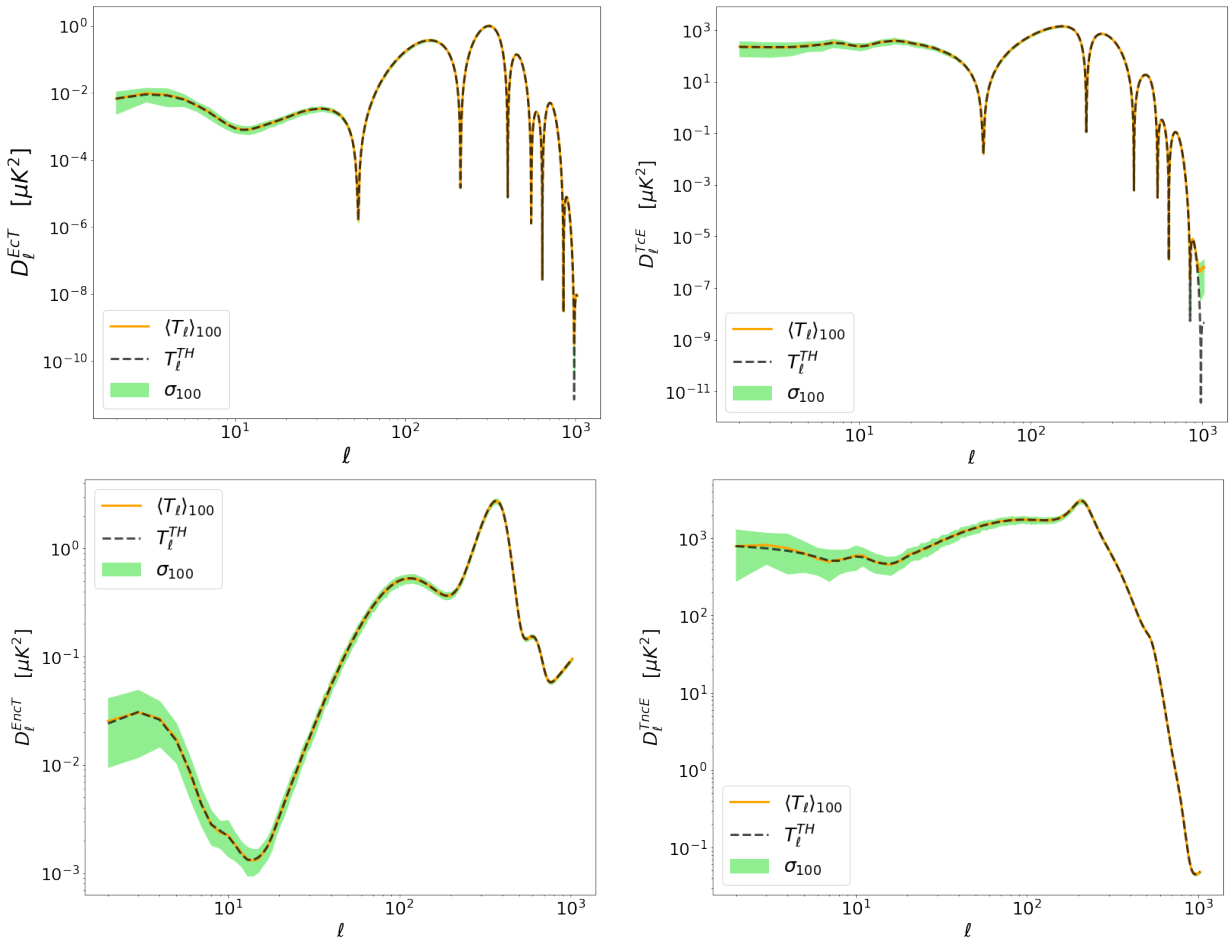

Figure 23: From CMB and noise simulated maps, we obtain the correlated and uncorrelated parts for the temperature and E-mode polarization maps. We can see the theoretical result obtained with `CAMB` (dashed line), the mean over 100 simulations (solid line) and the standard deviation (shaded).

3.3 Correlated maps from masked CMB & noise simulations

As we have seen in section §2.3, when computing the angular power spectrum on a masked map it creates coupling among different scales. Therefore, the angular power spectrum at large scales can contaminate the angular power spectrum at smaller scales. We have chosen `NaMaster` as our angular power spectrum estimator but we need to study the different filter calculation pipelines to obtain the optimal correlated and uncorrelated maps. We explore the difference between computing the spectra of the masked correlated and uncorrelated maps with the pseudo$-C_\ell$ algorithm and obtaining the spectra involved in the filter definition. In the first case, the intention is to recover the genuine angular power spectra and correct the effect of masking. However, in the second case the influence of the mask is taken into account in the angular power spectra used to calculate the filters, as it will be used to analyse masked maps. This opens two possibilities for determining the angular power spectrum of the masked maps which will constitute the filter, `healpy.anafast` or `NaMaster`. Once we have the angular power spectrum for each simulation we can get the average value of them or determine the first 100 filters and at the end average them. This leads to four possible filters we need to consider. The different possibilities for the definition of the filter are summarized in Figure 24.

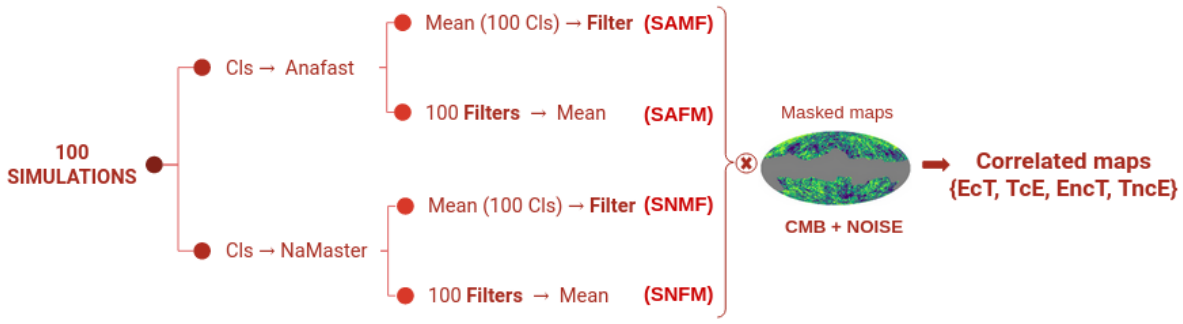

Figure 24: Scheme that describes the procedure that we will apply to determine which is the optimal way of defining the Wiener filters. The names are given by the initials of the different steps taken (e. g., 100 simulations (S) + C_ℓ with `anafast` (A) + $\langle C_\ell \rangle_{100}$ (M) + filter definition (F) $\equiv$ SAMF).

We represent them together with the full-sky theoretical filter defined in equation (3.3), henceforth theoretical filter, in Figure 25.

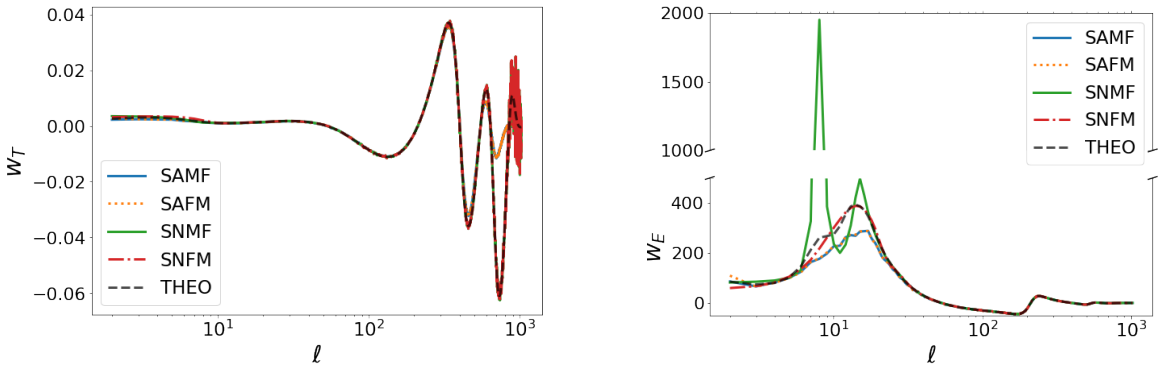

Figure 25: From masked CMB and noise simulated maps we obtain the four possibilities for defining the Wiener filter (SAMF, SAFM, SNMF, SNFM) together with the theoretical filter (dashed line).

As we can see, the results of the two `anafast` filters are almost identical, it does not matter the order in which we calculate the average. On the other hand, for the `NaMaster` filters we can clearly notice that it is better to perform the interpolation and the mean after computing the filter for the w_ℓ^E filter. To determine if these impressions are correct and moreover, which is the best filter, we need to compute the correlated and uncorrelated maps. We will compare them with the ideally

obtained from full-sky maps and with the theoretical filter, from now on ideal correlated maps, by calculating its difference with the corresponding maps obtained from the simulations. The residual maps obtained from these differences are only evaluated in the unmasked pixels. Afterwards, the dispersion of each difference map is computed, leading to a distribution of relative dispersions with respect to the ideal correlated maps. This will characterize how well we are able to recover the signal from masked maps. In Table 3 we present the most probable value of these distributions and the intervals that provide a 68% confidence level.

	EcT	TcE	$EncT$	$TncE$
THEO	$0.1435^{+0.0027}_{-0.0031}$	$0.240^{+0.019}_{-0.037}$	$0.0761^{+0.0014}_{-0.0018}$	$0.134^{+0.013}_{-0.020}$
SAMF	$0.1377^{+0.0011}_{-0.0061}$	$0.240^{+0.015}_{-0.023}$	$0.07329^{+0.00056}_{-0.00345}$	$0.1338^{+0.0068}_{-0.0201}$
SAFM	$0.1380^{+0.0011}_{-0.0061}$	$0.245^{+0.018}_{-0.024}$	$0.07362^{+0.00078}_{-0.00203}$	$0.1372^{+0.0092}_{-0.0169}$
SNMF	$0.1458^{+0.0030}_{-0.0029}$	$0.250^{+0.025}_{-0.030}$	$0.0774^{+0.0013}_{-0.0017}$	$0.140^{+0.015}_{-0.017}$
SNFM	$0.1453^{+0.0027}_{-0.0031}$	$0.90^{+0.15}_{-0.17}$	$0.0771^{+0.0017}_{-0.0015}$	$0.500^{+0.087}_{-0.084}$

Table 3: Relative dispersions obtained from the residual maps with a 68% confidence level.

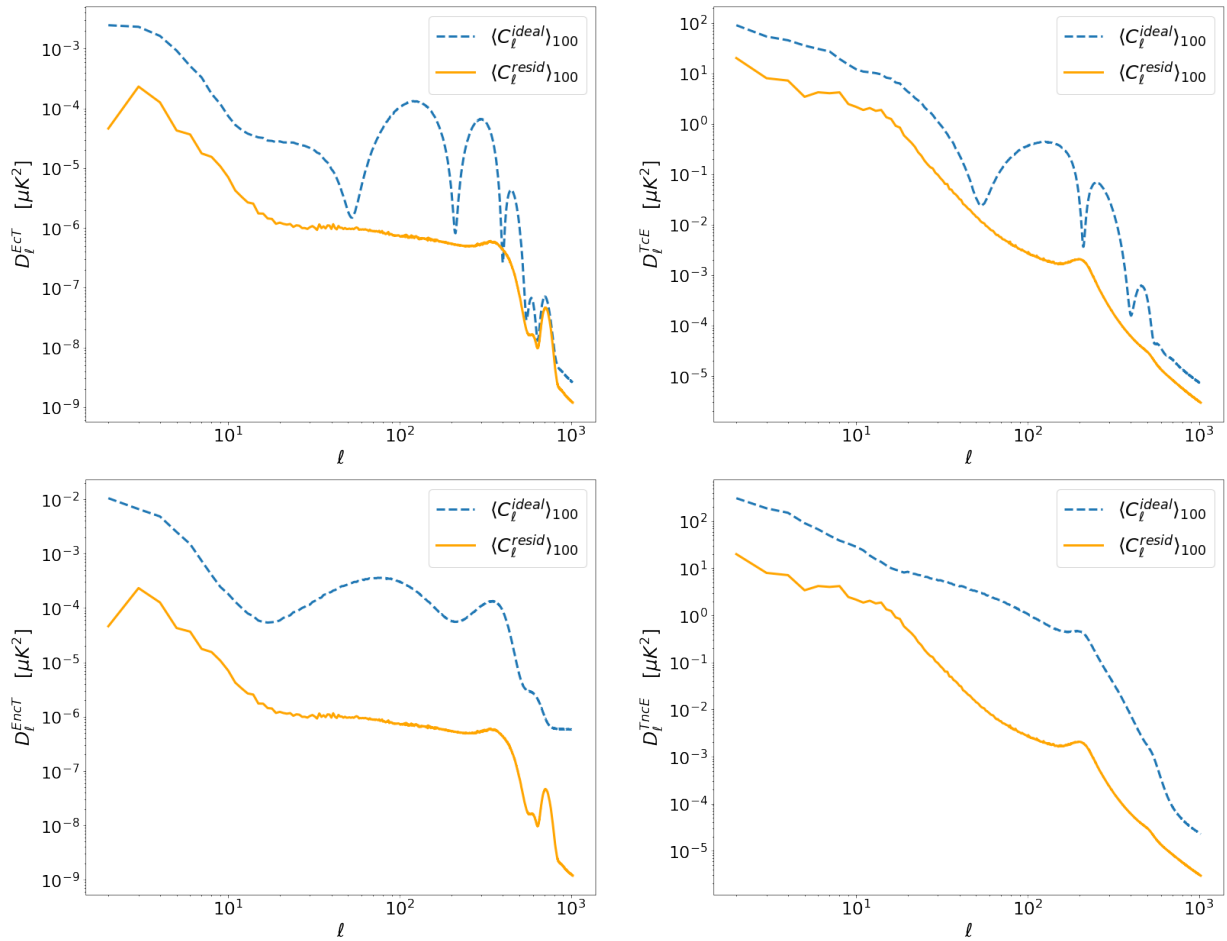

Figure 26: We can see the angular power spectra of full-sky correlated maps obtained with the theoretical filter in dashed line, $\langle C_\ell^{ideal}\rangle_{100}$, and of the residual maps for the SAFM filter in solid line, $\langle C_\ell^{resid}\rangle_{100}$.

Looking at these results we can confirm our first hypothesis. There is no significant difference between computing the average of 100 angular power spectra or 100 filters when they are determined with `anafast`. For the case of the `NaMaster` filters we can see that the EcT and $EncT$ are recovered with similar precision but there is much error committed with the temperature correlated maps for the SNMF filter, that is related with the outlier shown in Figure 25. Summing up all the information, we choose as our first filter option the SAFM, obtained with 100 simulations of masked CMB and noise maps, computing the spectra with `healpy.anafast` and obtaining the mean value of the 100 filters. The result seems to be consistent as it shows that the filter needs to be affected by the same complications as the analysed maps. In this particular case, with the `anafast` filters no mask corrections have been applied, unlike the `NaMaster` ones.

Finally, we compute the spectra of the ideal maps and the residual maps obtained with the best, SAFM, filter to visualize how the signal is recovered depending on the multipole. This is shown in Figure 26 and we can see that the power spectra of the residual maps is around two orders of magnitude below the ideal angular power spectra showing that the introduced relative error is $\sim 10\%$.

3.4 Data case

Until this point we have studied a set of 100 simulations from which we have obtained the Wiener filter and the corresponding correlated maps. As our purpose is to analyse the forthcoming observations obtained with LiteBIRD we need to extract conclusions from a single realization as we can only take measurements of one universe (our Universe). Also, experimentally the total map might have contributions from sources that lack an angular power spectrum model (e.g., residual and systematic foregrounds). The angular power spectrum of a given observation fluctuates around the expected value so we will need to estimate a smooth version of them that better resembles the underlying model. To reach our objective, we perform a binning of the multipoles followed by an interpolation to reduce the noise.

Firstly, we can study full-sky CMB and noise simulations trying to recover the theoretical prediction. We show the result of these smoothed angular power spectra, C_ℓ^{Smooth}, together with the theoretical prediction, C_ℓ^{TH} and a single realization obtained with `anafast`, C_ℓ^{Anaf}, in Figure 27.

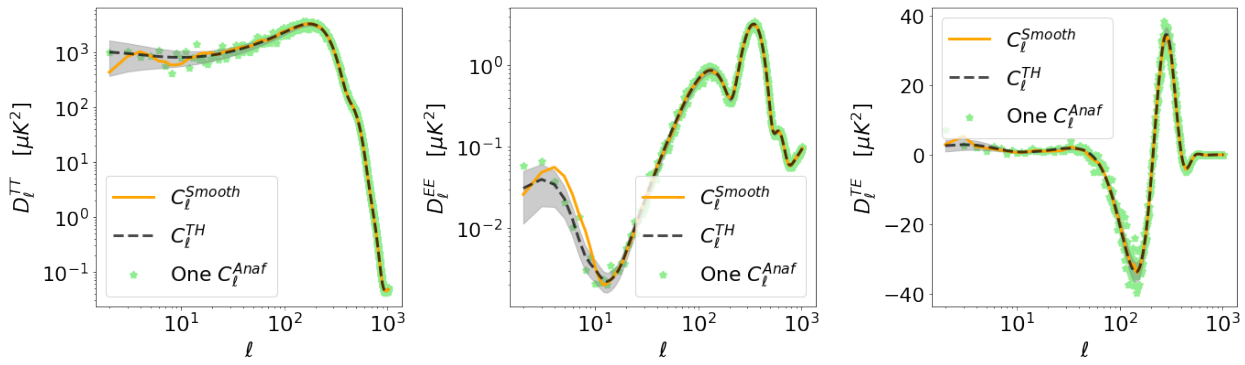

Figure 27: Angular power spectra obtained by smoothing (solid line), C_ℓ^{Smooth}, a realization of CMB and noise, One C_ℓ^{Anaf}. We include the theoretical models given by `CAMB` and by equation (1.19) for the CMB and the noise respectively in dashed.

We can see that we are able to obtain a smooth curve from one CMB and noise realization for all the multipole range although at low values, where the cosmic variance is higher, it is more difficult to obtain the theoretical prediction. With these smoothed angular power spectra we can compute the Wiener filter and compare it with the theoretical filter defined in equation (3.3) in Figure 28.

Secondly, we need to analyse masked CMB and noise simulations and see if we are able to recover the theoretical estimations with the smoothing method. In an analogous way as we have done in

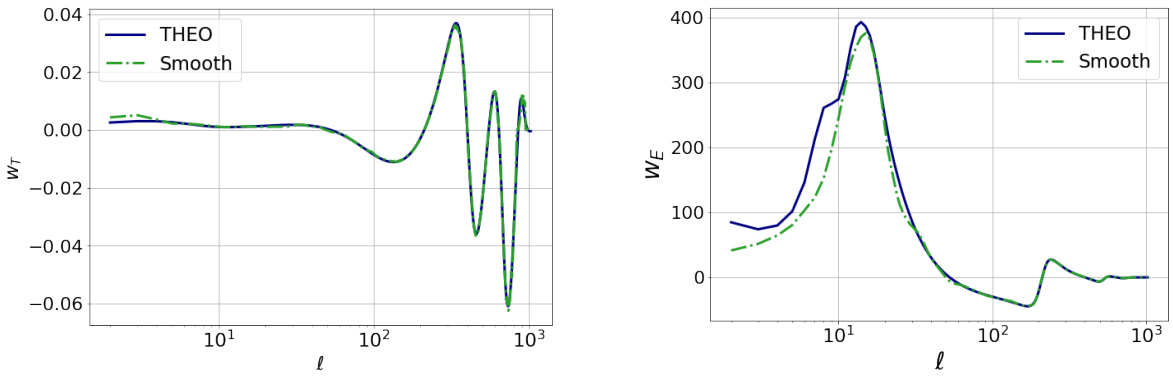

Figure 28: Wiener filters for CMB and noise maps. The solid line represents the theoretical filter given by equation (3.3) and the dashed line represents the smooth filter from one realization.

section §3.3 we need to find the best filter definition when a mask is included. This leads to four possible filters that are summarized in Figure 29.

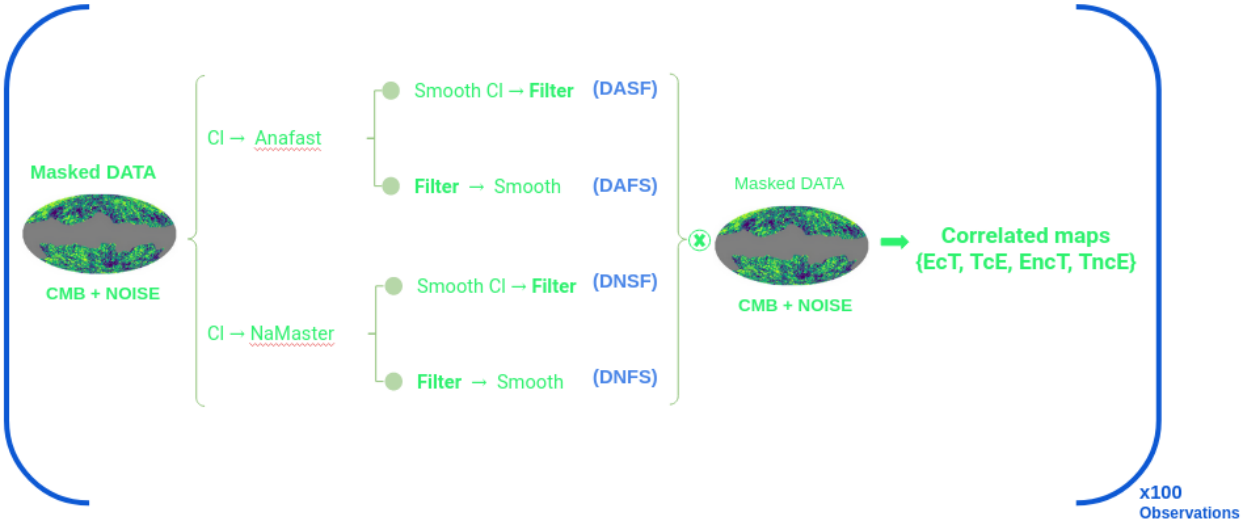

Figure 29: Scheme that describes the procedure that we will apply to determine which is the optimal way of defining the Wiener filters. The names are given by the initials of the different steps taken (e. g., Data (D) + C_ℓ with `anafast` (A) + Smooth method (S) + filter definition (F) ≡ DASF).

We represent them together with the theoretical filter in Figure 30. We can see that for the temperature filters there is a difference between the `anafast` and `NaMaster` results at large ℓ values, where we can appreciate the masking effects. For the E-mode polarization filters, better results seem to be obtained when the angular power spectra computation is performed with `NaMaster` and the smoothing is applied after the filter calculation. However, we do not know which is the best filter definition and so we need to quantify these differences. This is done by obtaining the correlated and uncorrelated maps and then calculating the relative dispersions associated to the residual maps as we have done in section §3.3. This results are outlined in Table 4 where we have also included the raw filters defined with the spectra without applying the smooth method to see if there is an improvement (DAF/DNF ≡ Data (D) + C_ℓ with `anafast`/`NaMaster` (A/N) + filter definition (F)).

Certainly, we can see there is an improvement when applying the smoothing method either to the spectrum or to the filter. Not only that but we can see that the best results for all the correlated maps is obtained with the DAFS filter, which implies that the best combination is to compute the spectrum of the masked maps with `anafast` and subsequently applying the smoothing method once the filter has been obtained.

In a similar way as we concluded with the simulation procedure, it seems that it is better to define the filter containing the same complications of the analysed maps (i.e., not performing any

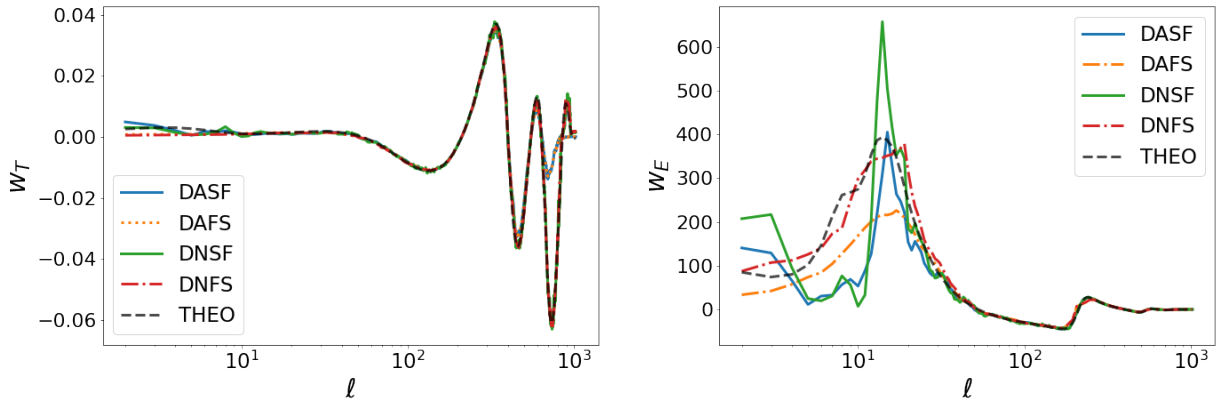

Figure 30: From masked CMB and noise simulated maps, we obtain the four possibilities for defining the Wiener filter (DASF, DAFS, DNSF, DNFS) together with the theoretical filter (dashed line).

	EcT	TcE	$EncT$	$TncE$
DAFS	$0.1598^{+0.0073}_{-0.0059}$	$0.284^{+0.021}_{-0.036}$	$0.0848^{+0.0035}_{-0.0033}$	$0.162^{+0.015}_{-0.019}$
DASF	$0.1468^{+0.0021}_{-0.0080}$	$0.335^{+0.023}_{-0.059}$	$0.0779^{+0.0012}_{-0.0043}$	$0.1867^{+0.0088}_{-0.0345}$
DAF	$0.1668^{+0.0028}_{-0.0090}$	$0.320^{+0.022}_{-0.063}$	$0.0894^{+0.0021}_{-0.0045}$	$0.181^{+0.015}_{-0.037}$
DNFS	$0.165^{+0.043}_{-0.091}$	$0.50^{+0.96}_{-0.61}$	$0.088^{+0.021}_{-0.048}$	$0.27^{+0.39}_{-0.34}$
DNSF	$0.1602^{+0.0037}_{-0.0190}$	$0.421^{+0.065}_{-0.132}$	$0.0850^{+0.0019}_{-0.0106}$	$0.230^{+0.032}_{-0.075}$
DNF	$0.36^{+0.85}_{-0.55}$	$1.24^{+1.65}_{-2.37}$	$0.19^{+0.17}_{-0.29}$	$0.75^{+1.65}_{-1.32}$

Table 4: Relative dispersions obtained from the residual maps from 100 masked CMB and noise observations with a 68% confidence level.

mask correction on the spectra that contribute to filter definition). Moreover we have determined the angular power spectra of the residual maps to visualize the relative dispersions depending on the multipole allowing us to determine which ℓ contributes most to the error (see Figure 31).

3.5 Correlated maps from masked CMB, noise & foreground simulations

When there is foreground emission we do not have a reliable theoretical model to describe their angular power spectra. Therefore, as we have seen previously in section §3.4, we need to get a smooth curve from the observations to construct the Wiener filter. In the previous section we have determined the best way of constructing the Wiener filter to recover the optimal signal from observations and we will use this result to analyse the most general case, i.e., where foreground residuals are included. It is important to bear in mind that for missions (e.g., LiteBIRD) where the noise level is higher than the foreground residual we can neglect their impact on the analysis. Recalling the fact that the residual foreground level we are considering is almost negligible as we have seen in sections §2.4 and §2.5, the same result as for masked CMB and noise observations is expected. Not only that but we can assume the model generated with CMB and noise simulations to analyse maps affected with foregrounds to see if there is any noticeable difference. We will define two filters to perform the analysis, the first one obtained from a single realization including foreground residuals (DAFS_foreg), and the second one will be the previously simulated SAFM filter which neglects the foreground contribution. Following the same procedure as in previous sections we present the results for the relative dispersions obtained from the residual maps in Table 5.

As we can see neglecting the foregrounds to generate the simulated model we obtain better results with the simulation approach when the foreground residuals level is negligible, as expected. However, in order to quantify the amplitude at which these residual foregrounds are relevant to

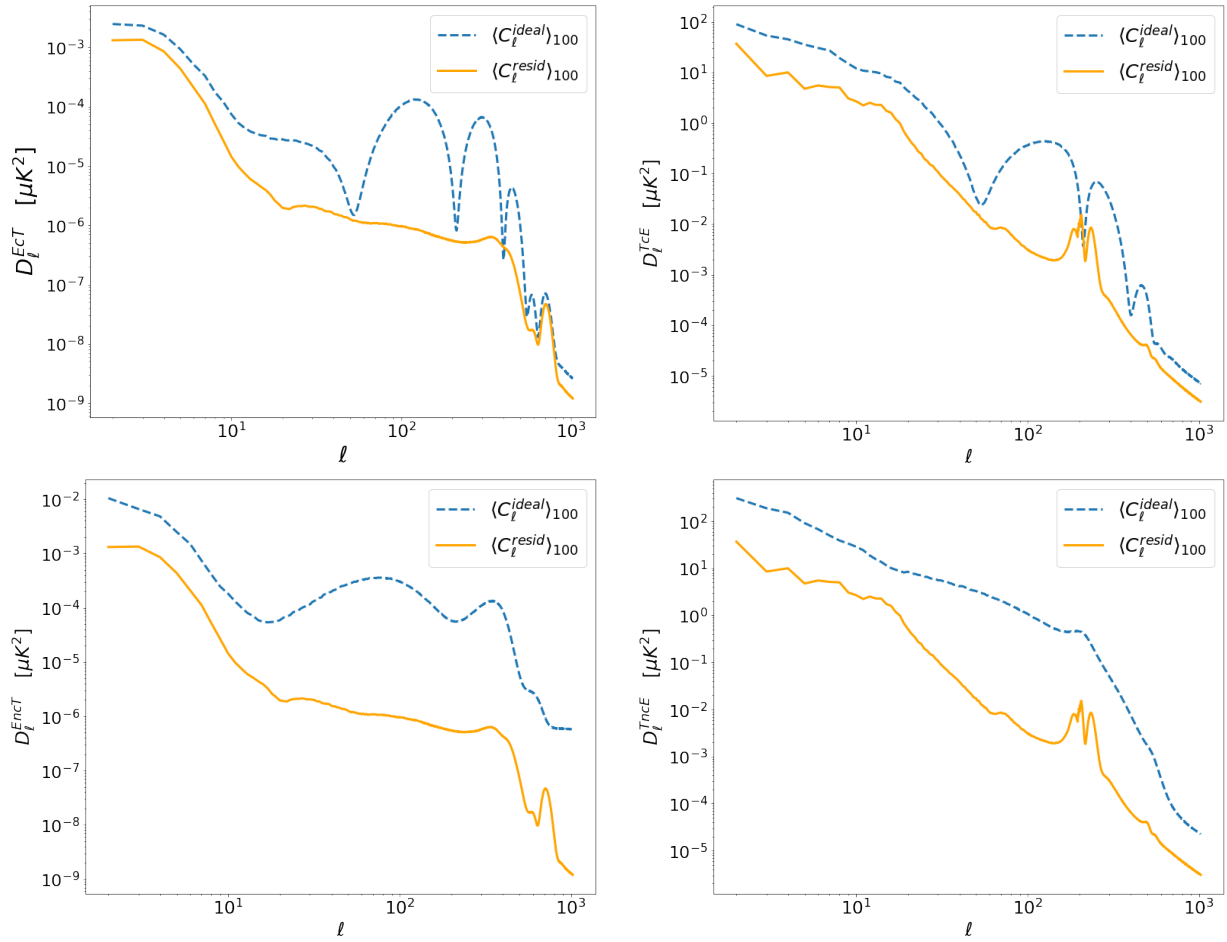

Figure 31: We can see the angular power spectra of full-sky correlated maps obtained with the theoretical filter in dashed line, $\langle C_\ell^{ideal}\rangle_{100}$, and of the residual maps for the DAFS filter in solid line, $\langle C_\ell^{resid}\rangle_{100}$.

	EcT	TcE	$EncT$	$TncE$
DAFS_foreg	$0.1596^{+0.0067}_{-0.0065}$	$0.284^{+0.021}_{-0.040}$	$0.0849^{+0.0036}_{-0.0035}$	$0.163^{+0.017}_{-0.018}$
SAFM	$0.13771^{+0.00011}_{-0.00609}$	$0.241^{+0.012}_{-0.029}$	$0.07339^{+0.00077}_{-0.00255}$	$0.1344^{+0.0084}_{-0.0205}$

Table 5: Relative dispersions obtained from the residual maps from 100 masked CMB, noise and foreground observations with 68% confidence level.

be included in the analysis we perform the same procedure but increasing the contribution of the foregrounds by factors $\{10, 50, 100\}$. We determine the relative dispersions of the residual maps for the different cases and we show the results in Table 6.

We can clearly notice the differences when the foreground residual contribution increases, mainly in the temperature correlated and uncorrelated maps. Not only that, but we can observe the importance of defining a filter from the observations, in this case including foreground residual, as they mitigate the relative error committed on the recovery of the temperature maps. For the E-mode correlated and uncorrelated maps the effect is not so noticeable as the foreground residual may have less contribution. For these maps both procedures return similar results.

	EcT	TcE	$EncT$	$TncE$
DAFS_foreg (x10)	$0.1579^{+0.0046}_{-0.0078}$	$0.300^{+0.019}_{-0.053}$	$0.08835^{+0.0025}_{-0.0064}$	$0.176^{+0.016}_{-0.026}$
DAFS_foreg (x50)	$0.1564^{+0.0033}_{-0.0109}$	$0.507^{+0.026}_{-0.044}$	$0.1839^{+0.0045}_{-0.0094}$	$0.284^{+0.012}_{-0.028}$
DAFS_foreg (x100)	$0.1569^{+0.0028}_{-0.0114}$	$0.589^{+0.018}_{-0.042}$	$0.4389^{+0.0054}_{-0.0067}$	$0.336^{+0.013}_{-0.040}$
SAFM (x10)	$0.13767^{+0.00091}_{-0.00613}$	$0.261^{+0.011}_{-0.064}$	$0.0800^{+0.0027}_{-0.0013}$	$0.1449^{+0.0081}_{-0.0412}$
SAFM (x50)	$0.1382^{+0.0011}_{-0.0063}$	$0.708^{+0.037}_{-0.076}$	$0.1789^{+0.0035}_{-0.0023}$	$0.397^{+0.023}_{-0.055}$
SAFM (x100)	$0.1415^{+0.0017}_{-0.0033}$	$1.773^{+0.040}_{-0.108}$	$0.4348^{+0.0036}_{-0.0022}$	$1.027^{+0.058}_{-0.034}$

Table 6: Relative dispersions obtained from the residual maps from 100 masked CMB, noise and foreground observations with 68% confidence level.

4 Application to a Toy Model: Lack of power Anomaly

As introduced in section §1, a surprisingly small quadrupole moment was already found with the COBE data. Posterior missions, latter confirmed this detection and extended towards larger values of ℓ (WMAP and PLanck), and it is usually known as the "lack of power at large-scale" anomaly. In the multipole range $\ell \sim (0-30)$ we can notice that the observations are systematically below the model (see Figure 3). There are several premises that could explain the origin of this anomaly. The most interesting one would be that this anomaly has a primordial origin which could imply new early Universe physics. Another explanation would be that this anomaly could be a simple statistical fluctuation. We are going to make use of the method developed in previous sections in order to try to elucidate the origin of this anomaly. For that purpose, we perform a set of simulations including the lack of power anomaly in temperature maps as measured by Planck. On the other hand, we analyse different scenarios of the E-mode where we introduce an anomalous lack of power in its angular power spectrum. With these full-sky realizations, that are considered from now on as our observations, we obtain the correlated and uncorrelated maps by applying the theoretical filter.

Since ΛCDM only provides a model of the CMB angular power spectra, we need to quantify the goodness of the fit of our observations with respect to ΛCDM. We are going to test how probable it is to obtain our observations assuming ΛCDM. We will compute the p-value of our observations, meaning a value close to 0 or 1 an anomalous result.

Our purpose is to characterize the significance of the lack of power anomaly, which describes the systematic reduction of the power in the multipole range $\ell \sim (0-30)$. We compare our simulated observation with a set of 1000 simulations generated using ΛCDM model. The observation is simulated with `healpy` for which it is necessary to express the $a_{\ell m}$'s coefficients of the maps in terms of the power spectra. As we have Planck data available for the temperature angular power spectrum and T-E cross-angular power spectrum, we use them to include the anomaly in our simulation mimicking the observed behaviour. We rename the measured Planck angular power spectra as $C_\ell^{\rm Plank} \equiv \hat{C}_\ell$ and the predicted by ΛCDM model as $C_\ell^{\rm CAMB} \equiv C_\ell$. With this we have the following spherical harmonic coefficients:

$$t_{\ell m} = \eta_1 \sqrt{\hat{C}_\ell^{TT}}, \quad e_{\ell m} = \eta_1 \frac{\hat{C}_\ell^{TE}}{\sqrt{\hat{C}_\ell^{TT}}} + \eta_2 D_\ell, \quad b_{\ell m} = \eta_3 \sqrt{C_\ell^{BB}}, \tag{4.1}$$

where

$$\eta_1, \eta_2, \eta_3 \in \mathbb{C} : \left\{ \begin{array}{l} \sqrt{2}\mathrm{Re}(\eta_j) \sim \mathcal{N}(0,1) \\ \sqrt{2}\mathrm{Im}(\eta_j) \sim \mathcal{N}(0,1) \end{array} \right. . \tag{4.2}$$

and $\hat{C}_\ell^{TE}/\sqrt{\hat{C}_\ell^{TT}}$ and D_ℓ are the correlated and uncorrelated parts of the E-mode with the temperature respectively. To be consistent with ΛCDM model we need to compute the E-mode polarization spectrum defining D_ℓ as:

$$D_\ell = \sqrt{C_\ell^{EE} - \frac{(C_\ell^{TE})^2}{C_\ell^{TT}}} \ . \tag{4.3}$$

These $a_{\ell m}$'s and η_j coefficients satisfy that:

$$t_{\ell m}^* = (-1)^m t_{\ell m}, \ e_{\ell m}^* = (-1)^m e_{\ell m}, \ b_{\ell m}^* = (-1)^m b_{\ell m}, \tag{4.4}$$

$$\langle \eta_j \eta_j^* \rangle = \langle \left(\eta_j^r + i\eta_j^i\right)\left(\eta_j^r - i\eta_j^i\right) \rangle = \langle \eta_j^r \eta_j^r \rangle + \langle \eta_j^i \eta_j^i \rangle = \frac{1}{2} + \frac{1}{2} = 1, \tag{4.5}$$

and so the power spectra is obtained as expected:

$$\langle t_{\ell m} t_{\ell m}^* \rangle = \hat{C}_\ell^{TT}, \tag{4.6}$$

$$\langle e_{\ell m} e_{\ell m}^* \rangle = \frac{(\hat{C}_\ell^{TE})^2}{\hat{C}_\ell^{TT}} + D_\ell^2 = \tilde{C}_\ell^{EE}, \tag{4.7}$$

$$\langle b_{\ell m} b_{\ell m}^* \rangle = C_\ell^{BB}. \tag{4.8}$$

With these definitions we modify the E-mode polarization spectrum using a factor to decrease its power at low multipoles. For this we define a parameter, $\alpha \in [0.1, 1]$. Therefore, this leads to a redefinition of the D_ℓ uncorrelated part of the E-mode power spectrum for each value of this parameter as:

$$D_\ell^2(\alpha) = \begin{cases} \alpha D_\ell^2 & , \quad \ell \leq 30 \\ \\ D_\ell^2 & , \quad \ell > 30 \end{cases} \tag{4.9}$$

where $\alpha = 1$ represents that the E-mode angular power spectrum remains compatible with ΛCDM. When α values are smaller than unity, this induces a lack of power in the E-mode angular power spectrum.

Once we have the observed TQU maps simulated we can compute the temperature/E-mode polarization correlated and uncorrelated maps with E-mode polarization/temperature. This leads to six maps (T, E, EcT, TcE, $EncT$ and $TncE$) we need to analyse. We compute the variance of these maps and compare them with the variances distribution given by the set of 1000 simulations. We represent the histograms obtained for these maps together with $\alpha = 1$, $\alpha = 0.1$ observations.

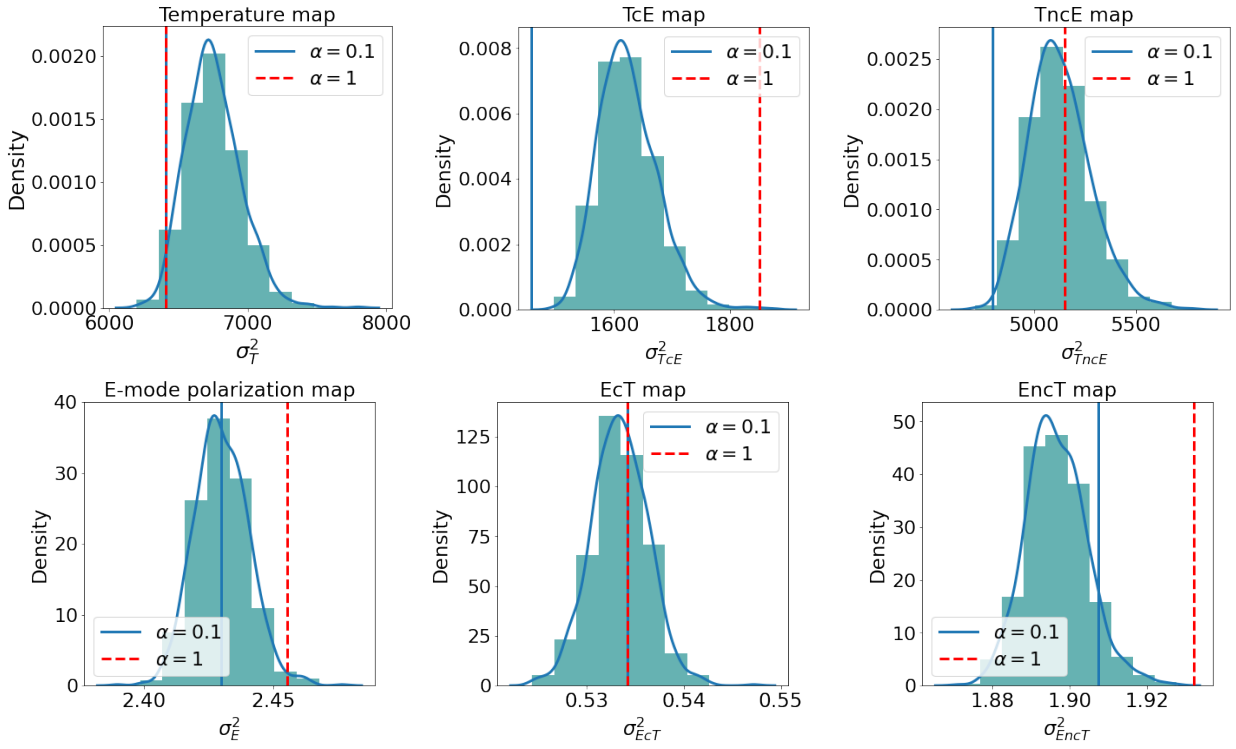

Figure 32: Histograms with the theoretical distribution given by a set of 1000 simulations and two observations ($\alpha = 0.1, 1$) assuming ΛCDM model.

As the dependence with α is only included in the C_ℓ^{EE} spectrum, we notice that the variance of the T and EcT are independent of the parameter. We observe that after applying the methodology developed during the work to obtain the correlated and uncorrelated maps, the p-value of the TcE and $EncT$ shows that the significance of the anomaly detection is improved in comparison with the original T and E maps. These two maps have angular power spectra proportional to C_ℓ^{EE} and so here we can notice the importance of future missions like LiteBIRD, which will retrieve an E map with uncertainties on the cosmic variance limit.

In Figure 33 we can see the change on the p-value depending on the level of anomaly included in the E-mode. Recalling that $\alpha = 1$ refers to the situation where the anomaly is only included in the temperature maps as measured by Planck, we can see that as we include the lack of power in the E-mode maps the variances of the maps change. If we focus on the TcE map, we have an anomalous

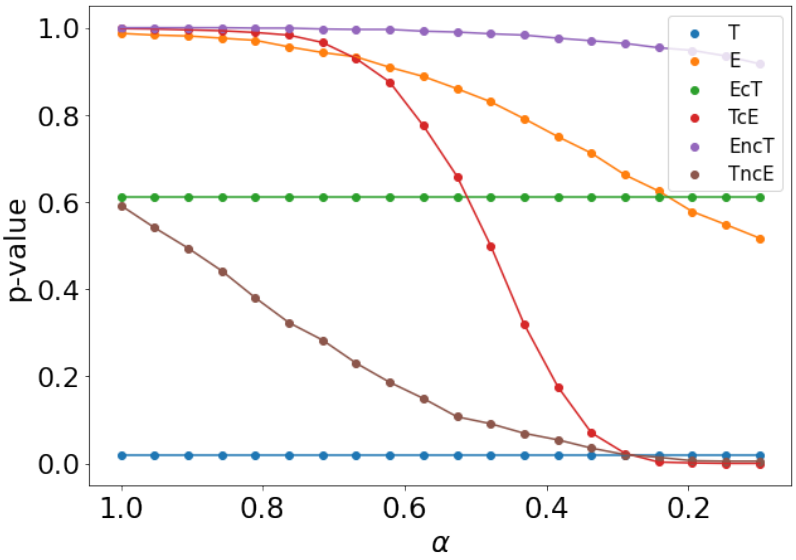

Figure 33: Evolution of the p-values for all the analysed maps with respect to the α parameter.

variance for $\alpha = 1$ but greater than the expected from ΛCDM, and as the anomaly in E-mode is included this variance becomes smaller being more compatible with the standard cosmological prediction ($\alpha \sim 0.5$). From this point the value of the variance continues decreasing, being more anomalous with respect to the theoretical prediction.

5 Conclusions

During this work we have developed a methodology based on Wiener filtering to obtain the correlated and uncorrelated maps of both temperature and E-mode polarization. Depending on the level of contaminants present in the simulations we had found different techniques to calculate the optimal Wiener filters. We have also analysed the difference between defining the filter from simulations, where a cosmological model is assumed, or from observations.

For the simulation approach, we have seen that there are different possibilities for the filter definition when a mask is included (§3.3) and that their effects are relevant in the filter construction. To know which filter recovers the optimal signal, we computed the relative dispersions, with respect to the ideal maps, of the difference residual maps. This leads us to state that there is no noticeable difference between computing the average before or after the `anafast` filters are defined but for `NaMaster` filters there is a clear disadvantage when the mean angular power spectrum is calculated before the filter definition. Overall, with the results shown in Table 3, the best filter is chosen to be the SAMF, which is computed from simulations (S), the angular power spectra is obtained with `anafast` (A), then the mean value of the 100 C_ℓ is performed (M) and finally we defined the filter (F).

For the data case, we had found a method for smoothing the angular power spectra of one realization that will be considered as our observation. In a similar way as in the simulation case, we have four different possibilities for the filter definition. We have compared the results with the relative dispersions of the difference residual maps and we got that the best filter is DAFS, computed from a single realization or data (D), the angular power spectra is obtained with `anafast` (A), then we define the filter (F) and finally we smooth it (S).

In section §3.5 we included the foreground residuals in the analysis bearing in mind that we do not have a model to describe their emission. As we have also mentioned, we have obtained foreground residual contributions according to [30, 28], which are negligible in comparison with the noise level. This allows us to analyse these CMB maps with the SAMF filter which did not consider any foreground contribution. Moreover, we obtained a filter like in the data case trying to compare the real influence of these foreground residuals in the filter definition (DAFS_foreg). As expected, we found better results for the simulated approach when the foreground residual level is negligible (see Table 5). To delve further into the importance of drawing conclusions from data we increased the foreground residual contribution by the following factors: $\{10, 50, 100\}$, to see whether there is a difference between the filter from simulations of the one derived from the data. As we can see in Table 6, the importance of having a method to calculate a filter from the data is remarkable for the temperature correlated and uncorrelated maps. We observed that when the residual foregrounds contribution is not negligible we can no longer use the filter obtained from simulations as we lack a reliable model of the residual foregrounds angular power spectrum. This degeneration is softened with the data strategy. For the E-mode correlated and uncorrelated maps both procedures return similar results.

Finally, we have applied the developed methodology to simulated maps with lack of power at low multipoles where we analysed whether more statistically significant conclusions can be drawn from the correlated and uncorrelated maps than from the raw maps. We generated 1000 simulations to obtain a distribution of the ΛCDM T, E, TcE, $TncE$, EcT and $EncT$ variance and we used them to test if our observation is compatible with ΛCDM. We computed the the p-value to determine if we would detect the anomaly with higher significance in the correlated and uncorrelated maps. In these simulated observations we included the observed lack of power anomaly, only in temperature as measured by Planck and studied different E-mode cases where we introduced the anomaly by decreasing the power in the low multipole range using an amplitude parameter α. We have seen that a more anomalous result is obtained for TcE and $EncT$ in comparisson with the raw T and E ones, and so this methology could help us detecting the lack of power anomaly with a higher significance in future missions.

Acknowledgments

LPM acknowledge partial financial support from the Severo Ochoa y Unidades María de Maeztu scholarship program of the Consejo Superior de Investigaciones Científicas (CSIC). We acknowledge Santander Supercomputacion support group at the University of Cantabria who provided access to the supercomputer Altamira Supercomputer at the Institute of Physics of Cantabria (IFCA-CSIC), member of the Spanish Supercomputing Network, for performing simulations. We have also made use of some Python packages such as `PySM` [26], `NaMaster` [24], `matplotlib`, `numpy` and `pandas` among others.

References

[1] D. J. Fixsen, ***The temperature of the Cosmic Microwave Background***, *The Astrophysical Journal*, (2009). http://dx.doi.org/10.1088/0004-637X/707/2/916.

[2] D. Samtleben, S. Staggs, and B. Winstein, ***The Cosmic Microwave Background for Pedestrians: A Review for Particle and Nuclear Physicists***, *Annual Review of Nuclear and Particle Science*, (2007). http://dx.doi.org/10.1146/annurev.nucl.54.070103.181232.

[3] A. Penzias and R. Wilson, ***A measurement of excess antenna temperature at 4080 Mc/s***, *The Astrophysical Journal*, (1965).

[4] Dicke et. al., ***Cosmic Black-Body Radiation.***, (1965). https://ui.adsabs.harvard.edu/abs/1965ApJ...142..414D.

[5] Wright, E. L. and Smoot, George F. and Bennett, C. L. and Lubin, P. M., ***Angular Power Spectrum of the Microwave Background Anisotropy seen by the COBE Differential Microwave Radiometer***, *Astrophys. J.*, vol. 436, pp. 443–451, (1994).

[6] George F. Smoot et. al., ***Structure in the COBE differential microwave radiometer first year maps***, *Astrophys. J. Lett.*, vol. 396, pp. L1–L5, (1992).

[7] C. L. Bennett, M. Halpern, G. Hinshaw, N. Jarosik, A. Kogut, M. Limon, S. S. Meyer, L. Page, D. N. Spergel, G. S. Tucker, and et al., ***First-Year Wilkinson Microwave Anisotropy Probe (WMAP) Observations: Preliminary Maps and Basic Results***, *The Astrophysical Journal Supplement Series*, no. 1, (2003). http://dx.doi.org/10.1086/377253.

[8] Planck Collaboration, ***Planck 2013 results. I. Overview of products and scientific results***, *Astronomy & Astrophysics*, (2014). http://dx.doi.org/10.1051/0004-6361/201321529.

[9] M. Tristram, A. J. Banday, K. M. Górski, R. Keskitalo, C. R. Lawrence, K. J. Andersen, R. B. Barreiro, J. Borrill, H. K. Eriksen, R. Fernandez-Cobos, and et al., ***Planck constraints on the tensor-to-scalar ratio***, *Astronomy & Astrophysics*, (2021). http://dx.doi.org/10.1051/0004-6361/202039585.

[10] Planck Collaboration, ***Planck 2018 results. VI. Cosmological parameters***, (2018).

[11] A. Challinor, ***CMB anisotropy science: a review***, *Proceedings of the International Astronomical Union*, (2012). http://dx.doi.org/10.1017/S1743921312016663.

[12] M. Kamionkowski, A. Kosowsky, and A. Stebbins, ***Statistics of cosmic microwave background polarization***, *Physical Review D*, vol. 55, no. 12, (1997). http://dx.doi.org/10.1103/PhysRevD.55.7368.

[13] A. Lewis and A. Challinor, ***CAMB: Code for Anisotropies in the Microwave Background***, *Astrophysiscs Source Code Library*, (2011).

[14] Andrea Zonca, Leo Singer, Daniel Lenz, Martin Reinecke, Cyrille Rosset, Eric Hivon, and Krzysztof Gorski, ***healpy: equal area pixelization and spherical harmonics transforms for data on the sphere in Python***, *Journal of Open Source Software*, (2019). https://doi.org/10.21105/joss.01298.

[15] K. M. Gorski, E. Hivon, A. J. Banday, B. D. Wandelt, F. K. Hansen, M. Reinecke, and M. Bartelmann, ***HEALPix: A Framework for High-Resolution Discretization and Fast Analysis of Data Distributed on the Sphere***, *The Astrophysical Journal*, no. 2, (2005). http://dx.doi.org/10.1086/427976.

[16] Kiyotomo Ichiki, ***CMB foreground: A concise review***, *Progress of Theoretical and Experimental Physics*, (2014). https://doi.org/10.1093/ptep/ptu065.

[17] Planck Collaboration, ***Planck 2015 results. X. Diffuse component separation: Foreground maps***, *Astronomy & Astrophysics*, (2016). http://dx.doi.org/10.1051/0004-6361/201525967.

[18] Planck Collaboration, ***Planck 2018 results. VII. Isotropy and Statistics of the CMB***, *Astronomy & Astrophysics*, (2020). http://dx.doi.org/10.1051/0004-6361/201935201.

[19] Planck Collaboration, ***Planck 2013 results. XXIII. Isotropy and statistics of the CMB***, *Astronomy & Astrophysics*, (2014). http://dx.doi.org/10.1051/0004-6361/201321534.

[20] D. Jeong and M. Kamionkowski, ***Gravitational Waves, CMB Polarization, and the Hubble Tension***, *Physical Review Letters*, (2020). http://dx.doi.org/10.1103/PhysRevLett.124.041301.

[21] M. Frommert and T. A. Ensslin, ***Ironing out primordial temperature fluctuations with polarisation: optimal detection of cosmic structure imprints***, (2009).

[22] M. Hazumi et. al., ***LiteBIRD: A Satellite for the Studies of B-Mode Polarization and Inflation from Cosmic Background Radiation Detection***, *J.Low Temp.Phys.*, vol. 194, no. 5-6, pp. 443–452, (2019). https://hal.archives-ouvertes.fr/hal-02136778.

[23] Hazumi, Masashi et. al, ***LiteBIRD satellite: JAXA's new strategic L-class mission for all-sky surveys of cosmic microwave background polarization***, *Space Telescopes and Instrumentation 2020: Optical, Infrared, and Millimeter Wave*, (2020). http://dx.doi.org/10.1117/12.2563050.

[24] D. Alonso, J. Sanchez, and A. Slosar, ***A unified pseudo-Cl framework***, *Monthly Notices of the Royal Astronomical Society*, vol. 484, p. 4127–4151, Jan 2019. http://dx.doi.org/10.1093/mnras/stz093.

[25] D. Scott, M. Srednicki, and M. White, ***"Sample variance" in small-scale cosmic microwave background anisotropy experiments***, *The Astrophysical Journal*, vol. 421, (1994). http://dx.doi.org/10.1086/187173.

[26] Ben Thorne, Joanna Dunkley, David Alonso, and Sigurd Naess, ***The Python Sky Model: software for simulating the Galactic microwave sky***, *Monthly Notices of the Royal Astronomical Society*, (2017). http://dx.doi.org/10.1093/mnras/stx949.

[27] J. Errard, S. M. Feeney, H. V. Peiris, and A. H. Jaffe, ***Robust forecasts on fundamental physics from the foreground-obscured, gravitationally-lensed CMB polarization***, *Journal of Cosmology and Astroparticle Physics*, (2016). http://dx.doi.org/10.1088/1475-7516/2016/03/052.

[28] P. Diego-Palazuelos, P. Vielva, E. Martínez-González, and R. Barreiro, ***Comparison of delensing methodologies and assessment of the delensing capabilities of future experiments***, *Journal of Cosmology and Astroparticle Physics*, (2020). http://dx.doi.org/10.1088/1475-7516/2020/11/058.

[29] Planck Collaboration, ***Planck 2015 results. XXI. The integrated Sachs-Wolfe effect***, *Astronomy & Astrophysics*, (2016). http://dx.doi.org/10.1051/0004-6361/201525831.

[30] J. Errard and R. Stompor, ***Characterizing bias on large scale CMB B-modes after Galactic foregrounds cleaning***, *Physical Review D*, Feb (2019). http://dx.doi.org/10.1103/PhysRevD.99.043529.

[31] M. Kamionkowski and E. D. Kovetz, ***The Quest for B Modes from Inflationary Gravitational Waves***, *Annual Review of Astronomy and Astrophysics*, (2016). http://dx.doi.org/10.1146/annurev-astro-081915-023433.

[32] T. L. Svalheim et. al., ***Beyond Planck XIV. Polarized foreground emission between 30 and 70 GHz***, (2020).

[33] Planck Collaboration, ***Planck intermediate results***, *Astronomy & Astrophysics*, (2020). http://dx.doi.org/10.1051/0004-6361/202038073.

[34] Planck Collaboration, ***Planck 2018 results. VIII. Gravitational lensing***, (2018).

[35] A. Lewis, ***CAMB Notes***, https://cosmologist.info/notes/CAMB.pdf.

[36] J. Delabrouille, M. Betoule, J.-B. Melin, M.-A. Miville-Deschênes, J. Gonzalez-Nuevo, M. Le Jeune, G. Castex, G. de Zotti, S. Basak, M. Ashdown, and et al., ***The pre-launch Planck Sky Model: a model of sky emission at submillimetre to centimetre wavelengths***, *Astronomy & Astrophysics*, (2013). http://dx.doi.org/10.1051/0004-6361/201220019.

[37] S. Dodelson, ***Modern Cosmology***. Amsterdam: Academic Press, (2003).